ADVANCING EARTH AND SPACE SCIENCES

JGR Solid Earth

RESEARCH ARTICLE
10.1029/2022JB026162

Crustal and Upper Mantle Velocity Structure of SE Tibet From Joint Inversion of Rayleigh Wave Phase Velocity and Teleseismic Body Wave Data

Xiaozhou Yang[1,2], Yinhe Luo[1,3], Chengxin Jiang[2], Yingjie Yang[4], Fenglin Niu[5], and Guoliang Li[6]

[1]Hubei Subsurface Multi-scale Imaging Key Laboratory, School of Geophysics and Geomatics, China University of Geosciences, Wuhan, China, [2]Research School of Earth Sciences, Australian National University, Canberra, ACT, Australia, [3]State Key Laboratory of Geological Processes and Mineral Resources, China University of Geosciences, Wuhan, China, [4]Department of Earth and Space Sciences, Southern University of Science and Technology, Shenzhen, China, [5]Department of Earth, Environmental and Planetary Sciences, Rice University, Houston, TX, USA, [6]Department of Earth Sciences and Southern California Earthquake Center, University of Southern California, Los Angeles, CA, USA

Key Points:

- A 3D velocity model of SE Tibet is obtained via a joint inversion of surface wave phase velocity and teleseismic body wave data
- Our model reveals spatial distributions of three isolated mid-lower crustal low-velocity zones with unprecedent details
- Broad low velocities in the upper mantle imply mantle upwelling related to the lithospheric delamination and slab subduction

Supporting Information:

Supporting Information may be found in the online version of this article.

Correspondence to:

Y. Luo and Y. Yang,
luoyinhe@cug.edu.cn;
yangyj@sustech.edu.cn

Citation:

Yang, X., Luo, Y., Jiang, C., Yang, Y., Niu, F., & Li, G. (2023). Crustal and upper mantle velocity structure of SE Tibet from joint inversion of Rayleigh wave phase velocity and teleseismic body wave data. *Journal of Geophysical Research: Solid Earth*, *128*, e2022JB026162. https://doi.org/10.1029/2022JB026162

Received 30 NOV 2022
Accepted 6 JUL 2023

Author Contributions:

Conceptualization: Xiaozhou Yang, Yinhe Luo, Chengxin Jiang, Yingjie Yang, Fenglin Niu
Data curation: Xiaozhou Yang, Chengxin Jiang, Fenglin Niu
Formal analysis: Yinhe Luo
Funding acquisition: Yinhe Luo, Chengxin Jiang, Yingjie Yang
Investigation: Xiaozhou Yang, Yinhe Luo, Guoliang Li
Methodology: Xiaozhou Yang, Yinhe Luo, Chengxin Jiang, Yingjie Yang, Fenglin Niu, Guoliang Li
Project Administration: Yinhe Luo, Fenglin Niu
Resources: Yingjie Yang, Fenglin Niu

Abstract Since the continental collision between the Indian and Eurasian plates began about 50 Ma ago, southeastern Tibet (SET) has undergone complex tectonic deformation. In this study, we investigate fine scale structural features of the crustal and upper mantle depths (<250 km) beneath SET, which hold important clues to understanding the dynamic processes related to this collision. A 3D shear velocity model is constructed through jointly inverting Rayleigh wave phase velocity and teleseismic body wave data from more than 650 stations. Our 3D model identifies three independent low-velocity zones (LVZs) in the mid-lower crust with unprecedented details. More specifically, we observe a prominent LVZ beneath the North Chuan-Dian Block, which is well separated from another LVZ beneath the Tengchong volcano in the south. This LVZ beneath the volcano represents a focused magma reservoir in the crust whose origin is potentially linked to the mantle upwelling associated with the eastward subduction of the Indian plate. The third LVZ, observed around the Xiaojiang Fault, likely represents a separated and mechanically weak layer in the mid-lower crust due to the combined effects of regional crustal thickening under the southeastward plateau expansion, mantle upwelling, and shear heating of strike-slip faults. In the upper mantle, we observe strong velocity reductions both in localized areas beneath the Tibetan Plateau and the broad region south of 26°N. These low velocity anomalies are sitting above high velocity anomalies at deeper depths, suggesting their association with lithospheric thickening and delamination processes.

Plain Language Summary Southeastern Tibet (SET) has undergone complex geological evolution due to the plate collision. To better understand the related dynamic processes, we present a high-resolution 3D S-wave velocity model from the earth surface to the depth of 250 km by using surface wave and body wave data. Our model shows three independent crustal low-velocity zones (LVZs). Especially, the one beneath the Tibetan Plateau is seen to be well separated from the one beneath the Tengchong volcano which represents the hot magma upwelling related to the eastward subduction of the Indian plate. In addition, another LVZ around the Xiaojiang Fault probably represents a separated and mechanically weak layer that is attributed to the regional crustal thickening under the southeastward plateau expansion, mantle upwelling, and shear heating of strike-slip faults. In the upper mantle, we observe strong velocity reductions both in localized areas beneath the Tibetan Plateau and the broad region south of 26°N. Many of these low velocity anomalies are sitting above high velocity anomalies at deeper depths, suggesting their origin of lithospheric thickening and delamination processes.

1. Introduction

The Tibetan Plateau is the world's largest and highest plateau resulting from the collision between the Indian and Eurasian plates that was initiated ~50 Ma ago (Molnar & Tapponnier, 1975; Rowley, 1996). The intensive collision, subduction and related deep dynamic processes create significant crustal shortening and uplifting of the Plateau, accompanied with eastward extrusion of plateau materials (Harrison et al., 1992; Yin & Harrison, 2000). Due to the strong blockage of the rigid Yangtze Craton (YC) in the east, southeastern Tibet (SET) serves as one of the most important channels for the escape of plateau materials (Cook & Royden, 2008). All these tectonic

Software: Xiaozhou Yang, Yinhe Luo, Chengxin Jiang, Guoliang Li
Supervision: Yinhe Luo, Chengxin Jiang, Yingjie Yang, Fenglin Niu
Validation: Xiaozhou Yang, Yinhe Luo, Yingjie Yang, Guoliang Li
Visualization: Xiaozhou Yang
Writing – original draft: Yinhe Luo
Writing – review & editing: Yinhe Luo, Chengxin Jiang, Yingjie Yang, Fenglin Niu, Guoliang Li

deformation and material transport processes have been imprinted in the crust and upper mantle depths; thus, its fine structure holds important clues to the understanding of the deformation mechanism of the plateau.

Two end-member models have been proposed to explain the growth of SET. These include (a) the rigid block extrusion model, in which the lithosphere extrudes along major strike-slip faults (Tapponnier et al., 1982, 2001), and (b) the middle and lower crustal channel flow model, in which weak crustal material flows viscously driven by lateral gravity gradient (Clark & Royden, 2000; Royden et al., 1997, 2008).

Various evidence exists to support both models. For example, GPS measurements reveal the entire SET is rotating clock-wisely around the Eastern Himalayan Syntaxis (EHS) through significant strike-slip motions along large fracture zones (e.g., Q. Wang, Zhang, et al., 2001; M. Wang & Shen, 2020; P. Z. Zhang et al., 2004). As the northern and eastern boundaries of the Chuan-Dian Block, the sinistral strike-slip Xianshuihe Fault (XSHF) and Xiaojiang Fault (XJF) are the most active two with slip rates of ∼10–11 and ∼7 mm/yr, respectively (Z.-K. Shen et al., 2005). The Lijiang–Xiaojinghe Fault (LXF), the largest fault within the Chuan-Dian Block, have a ∼3 mm/yr sinistral slip and a ∼1–2 mm/yr thrust slip (Hao et al., 2016; Z.-K. Shen et al., 2005). This indicates the strong interaction between rigid crustal blocks at shallow depths.

However, previous geophysical studies also find strong signatures for the existence of crustal channel flow at depth. For example, magnetotelluric images identify two high-conductivity channels in the middle and lower crust around the center of the Emeishan Large Igneous Province (ELIP) (Bai et al., 2010; X. Li et al., 2020). Lg-wave Q tomography reveals a low-Q zone in the deep crust extending from the Tibetan Plateau to the southeast, as well as an isolated low-Q zone located in the XJF (L.-F. Zhao et al., 2013). Terrestrial heat flow data of continental China show high values (>80 mW/m^2) at the SET (Hu et al., 2000; Jiang et al., 2019). Surface wave and body wave tomography also show significant low-velocity layers in the middle and lower crust (e.g., X. Bao, Song, & Li, 2015; M. Chen et al., 2014; Z. Huang et al., 2019; C. Y. Wang, Chan, & Mooney, 2003; Y. Yang et al., 2012; Y. Yang et al., 2020; Yao et al., 2008; Z. Zhang et al., 2020). The combination of the above geophysical signatures strongly suggests the existence of partial melt or low-viscosity mechanically weak zones in the middle and lower crust. On the other hand, relatively isolated and localized geophysical anomalies in the crust challenge the widespread and uniform channel flow model in SET, which leads to a growing consensus that the rigid block extrusion and channel flow models might work together to control the lithospheric deformation and material transport in the region (e.g., X. Bao, Sun, et al., 2015; Q. Y. Liu et al., 2014; Qiao et al., 2018; Y. Yang et al., 2020).

Nevertheless, differences in data and methodology used in previous studies have resulted in significant differences in resolved features, hindering the complete understanding on the connectivity of the detailed crustal flow patterns. For example, X. Bao, Sun, et al. (2015) suggest two parallel flow channels exist around the EHS with one from North Chuan-Dian Block (NCDB) to the Tengchong volcano and the other bypassing the ELIP and then turning southwest across the Red River Fault (RRF). M. Li et al. (2016) observe similar features in the north but suggest these two separated low-velocity channels probably merge again south of the ELIP. However, the more recent studies with broader and denser array coverage compared to the early generation models, such as Y. Yang et al. (2020), Z. Zhang et al. (2020) and Y. Liu, Yao, et al. (2021), all suggest that the crustal flow from the Tibetan Plateau is likely blocked by high velocity materials beneath the ELIP and therefore cannot flow further to the southeast. Therefore, the spatial distribution of crustal low-velocity zones (LVZs) and how they relate to major strike-slip faults at regional scales are still controversial, which is crucial for understanding material escape in the southeastern margin of the Tibetan Plateau and its extension. High-resolution regional geological and geophysical observations are necessary to provide further constraints on these processes.

Apart from crustal flows, the SET might also host possible channels for the extrusion of asthenosphere materials (M. Liu et al., 2004). Body wave traveltime tomography reveals extensive low-velocity anomalies in the uppermost mantle around the YC, which are interpreted as the southeastward mantle flow from the Tibetan Plateau (Z. Huang et al., 2015; Lei & Zhao, 2016). However, recent geochemical studies of Cenozoic potassic igneous rocks (B. Chen et al., 2017; Lu et al., 2015) as well as geophysical studies from reflected body waves (Feng et al., 2022), receiver functions (Xu et al., 2018; R. Zhang, Wu, et al., 2017) and teleseismic body wave traveltime tomography (Z. Huang et al., 2019) argue for an alternative mechanism of lithospheric delamination. They propose that the strong continental collision may lead to the thickening of the lithosphere and form higher-density lithosphere compared to the surrounding asthenosphere, promoting large-scale lithospheric delamination and mantle upwelling (Houseman et al., 1981; Schott & Schmeling, 1998). Moreover, the southern Yunnan region

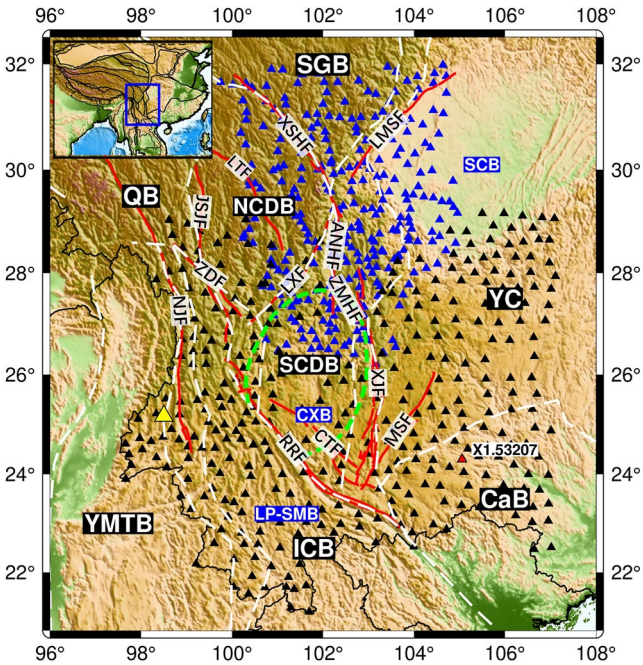

Figure 1. Main geological units and distribution of T1 (blue triangles) and X1 (black triangles) array. The yellow triangle denotes the Tengchong volcano zone. The green dashed line delineates the inner zone of ELIP. The white dashed lines delineate main geological units and the red solid lines represent faults (SGB, Songpan-Ganzi Block; QB, Qiangtang Block; YC, Yangtze Craton; CaB, Cathaysia Block; ICB, Indo-China Block; YMTB, Yunnan-Myanmar-Thailand Block; NCDB, North Chuan-Dian Block; SCDB, South Chuan-Dian Block; XSHF, Xianshuihe Fault; LMSF, Longmenshan Fault; ANHF, Anninghe Fault; ZMHF, Zemuhe Fault; XJF, Xiaojiang Fault; CTF, Chuxiong-Tonghai Fault; MSF, Mule-Shizong Fault; LXF, Lijiang-Xiaojinhe Fault; JSJF, Jinshajiang Fault; NJF, Nujiang Fault; ZDF, Zhongdian Fault; RRF, Red River Fault; LTF, Litang Fault; SCB, Sichuan Basin; CXB, Chuxiong Basin; LP-SMB, Lanping-Simao Basin).

has an east-west extensional dynamical background since the Late Miocene (G. Wang et al., 2008). Slab dehydration, breakup or mantle convection associated with the eastward subduction and rollback of the Indian plate beneath the Burma arc may also control the dynamic evolution of the SET (Guo et al., 2015; H. Y. Lee et al., 2016; Ni et al., 1989; Rao & Kalpna, 2005; Richards et al., 2007; C. Y. Wang et al., 2013). Geochemical studies of exposed mantle rocks and hydrothermal fluids indicate an important contribution of deep-source mantle dynamics processes to the expansion and uplift of the SET (B. Chen et al., 2017; M. Zhang et al., 2021). These processes will lead to different velocity features in the upper mantle. In this case, high resolution geophysical imaging results covering both crust and upper mantle depths are crucial to revealing the geometric relationships among the upper mantle low-velocity region, crustal channel flow, and surface fracture zones to explore possible crust-mantle interactions and geodynamic processes.

In this study, by taking advantage of the dense seismic arrays covering a broad region of the SET and their complex fault systems, we employ the ambient noise tomography (ANT) and teleseismic two-plane-wave tomography (TPWT) to obtain a broad period band of Rayleigh wave phase velocity data. We jointly invert these phase velocities and the teleseismic body-wave waveforms to further improve our constraints on the seismic discontinuities including the sedimentary bottom and Moho depths. Our 3D shear-wave velocity model shows unprecedented resolution compared to previous ones, offering new insights into the tectonic processes and intraplate volcanisms of the SET.

2. Data and Method

We collect continuous three-component seismic data from 303 broadband stations deployed in the western Sichuan region from October 2006 to July 2009 (T1 array; Q. Y. Liu et al., 2014) and also from 350 stations of the ChinArray-Himalaya Phase I project operating from May 2011 to December 2013 (X1 array; ChinArray, 2006). Both ambient noise and teleseismic data from the two arrays are used (Figure 1). Since the horizontal components of seismometers at some stations were misaligned during installation, we correct the azimuth of the two horizontal components according to the sensor orientations determined by Zeng et al. (2021) prior to data processing. The deviations of azimuthal angles are given in the supplementary material as Table S1 in Supporting Information S1.

2.1. Ambient Noise Tomography

We obtain Rayleigh wave phase velocity maps at periods of 5–50 s by performing ANT, and we briefly describe the data processing procedures below.

Following Bensen et al. (2007), we process the ambient noise data recorded on the vertical components from the selected stations and compute the cross-correlation functions (CCFs) among all available station pairs. To do that, we first decimate the continuous data from 20 Hz (for both arrays) to 1 Hz and cut them into one-day-long segments. For each daily segment, we remove the mean, the trend, the instrument response, and bandpass filter it at a period band of 3–100 s. We then apply a running-absolute-mean method in the time domain and spectrum whitening in the frequency domain to remove strong spurious signals such as earthquakes and to broaden the bandwidths, respectively. To improve the signal-to-noise ratios (SNRs) of the Rayleigh wave signals, we first linearly stack daily CCFs for each 5 days without overlapping, and then further stack the 5-day CCFs using a time-frequency domain phase-weighted stacking (tf-PWS) method (G. Li et al., 2018; Schimmel & Gallart, 2007). The nonlinear tf-PWS method has been proven to be very efficient in suppressing noise while retaining the dispersive characteristics of stacked waveforms (G. Li et al., 2018). Figure 2 shows some examples

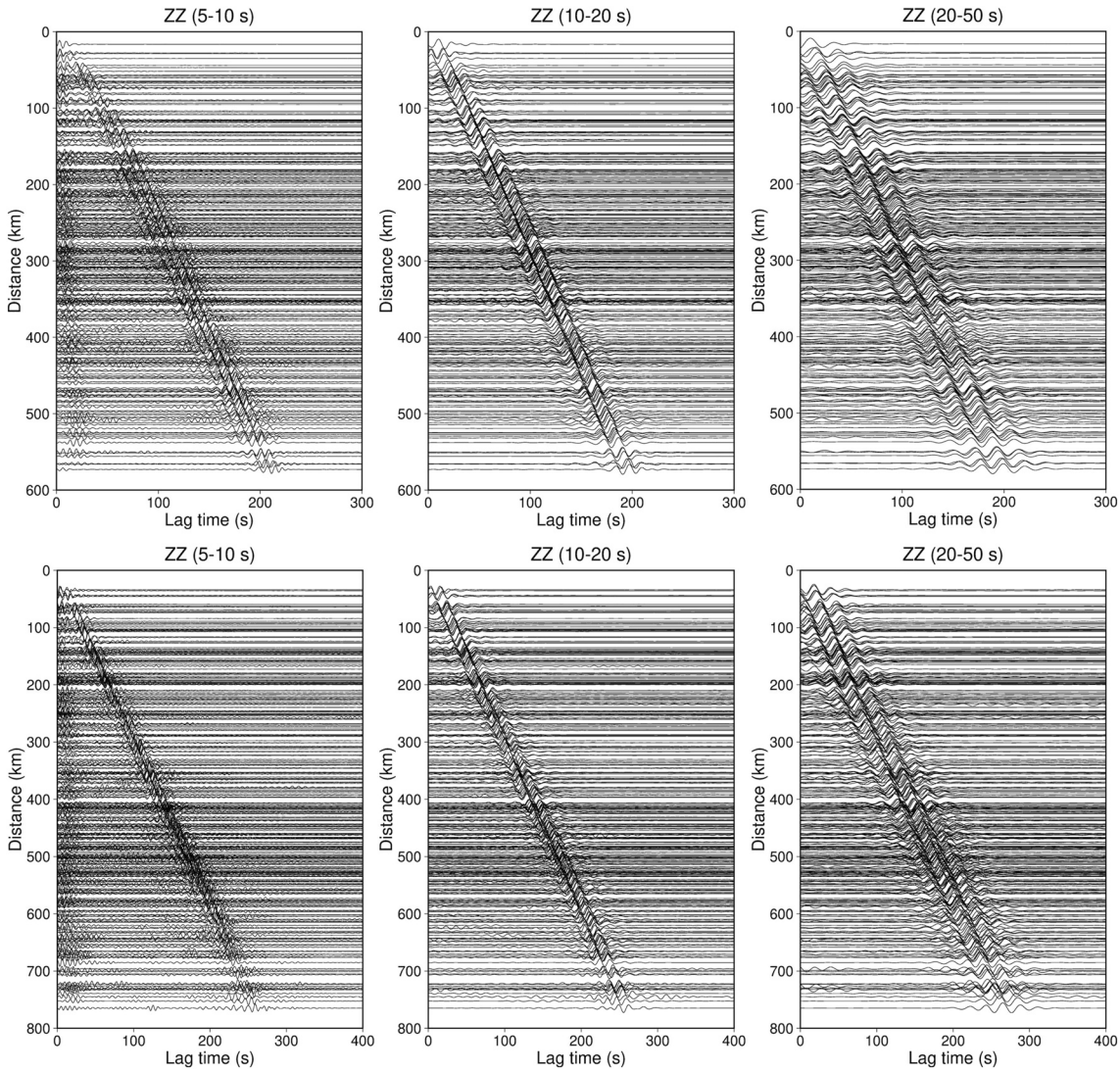

Figure 2. Vertical-component cross-correlation functions of T1 (top row) and X1 (bottom row) array at period bands of 5–10, 10–20, and 20–50 s.

of the vertical-component CCFs (ZZ) filtered at different period bands, which display clear move-outs of surface waves across the study region. Then, we adopt an automatic Frequency-Time Analysis method (FTAN) (Levshin & Ritzwoller, 2001) to measure Rayleigh wave phase velocity dispersion curves from all stacked CCFs. For quality control, we only retain measurements with SNRs greater than 10 and interstation distance longer than 1.5 wavelengths (Luo et al., 2015). Here, the SNR is defined as the ratio of the maximum amplitude of signal windows within a velocity range of 2–5 km/s to the root mean square of the trailing noise window of same length to the signal window. We then invert the obtained dispersion measurements for phase velocity maps at periods of 5–50 s using a ray-theory-based method of Barmin et al. (2001). In the inversion, we parameterize the study area using a $0.25° \times 0.25°$ grid. To remove the spurious inter-station dispersion measurements, we abandon those data with their phase travel time misfits larger than 6 s in the initial run of tomography, and then redo the tomography. Figure 3 demonstrates the constructed phase velocity maps at selected periods of 8, 20, 30, and 40 s from ANT. The relatively regular array geometry and large number of stations result in extremely dense ray path density covering a broad region of SET across different periods (see Figure S1 in Supporting Information S1).

2.2. Teleseismic Two-Plane-Wave Tomography

We further extract Rayleigh wave phase velocities at the intermediate/long period range (30–140 s) from teleseismic data and employ the teleseismic TPWT method based on a finite frequency theory (Forsyth & Li, 2005;

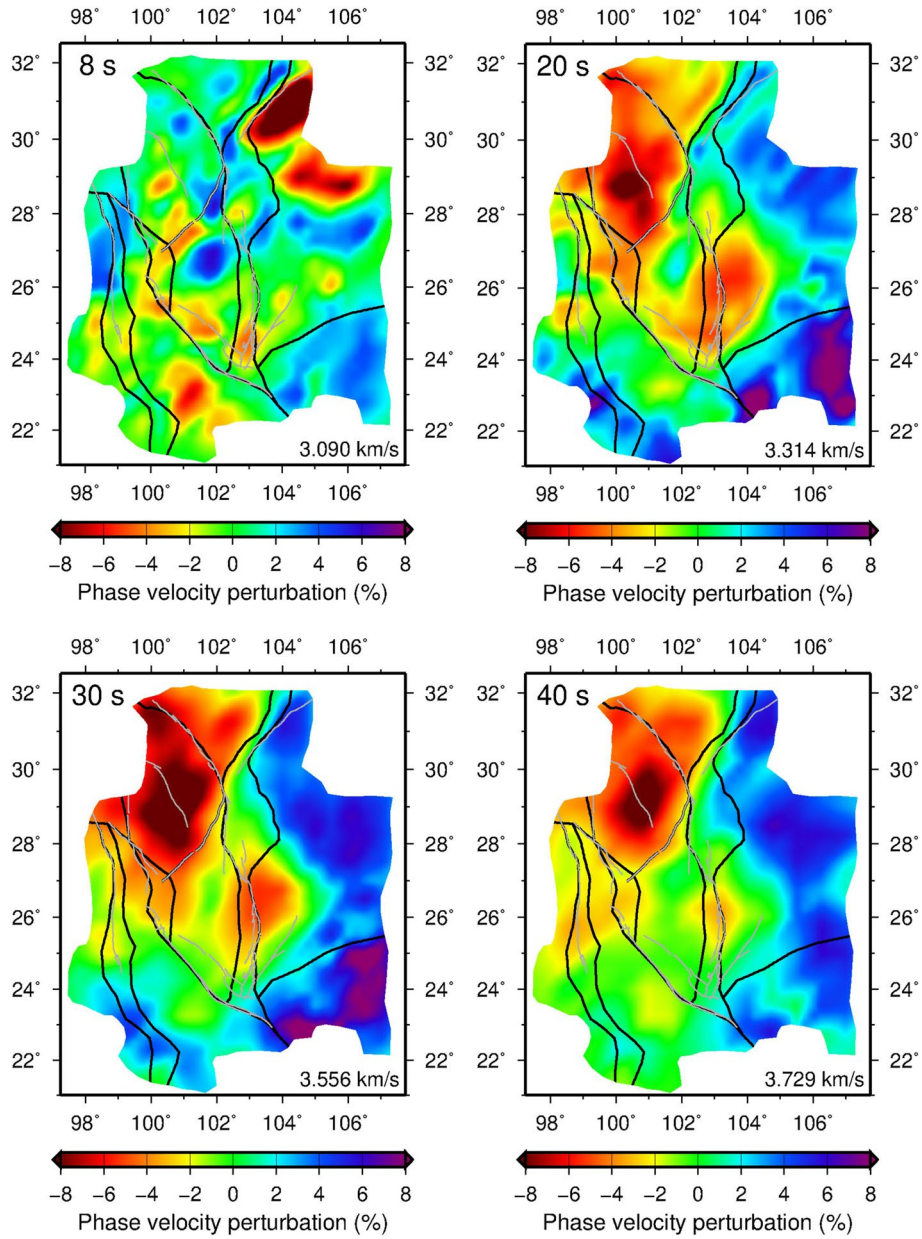

Figure 3. Phase velocity maps at different periods from ambient noise tomography.

Yang & Forsyth, 2006b) to construct phase velocity maps. The method of TPWT uses the interferences of two plane waves to simulate a complex surface wave wavefield resulting from each teleseismic event to account for multipathing and off-great-circle propagations of teleseismic surface waves. It employs 2-D Born approximation sensitivity kernels to represent the sensitivities of surface waves to velocity heterogeneities. The details of this method are described in Yang and Forsyth (2006a, 2006b) and we here only briefly describe the data processing procedures.

We first screen all the teleseismic events with $M_s > 5.5$ and epicenter distances of 30°–120° that occurred during the array deployment time based on the USGS catalog (https://earthquake.usgs.gov/earthquakes/search/). We isolate teleseismic waveforms from continuous seismic data using a 7,200 s long window starting from the event origin time. Only teleseismic events with SNR greater than 10 are retained for further analysis. A total of 416 high-quality events covering a broad azimuthal range are used for TPWT with their spatial distribution shown in Figure 4a. Figure 4b shows teleseismic waveforms from one example of the retained earthquakes, with clear surface wave energy traveling through the dense array. Both the phases and amplitudes of Rayleigh waves of

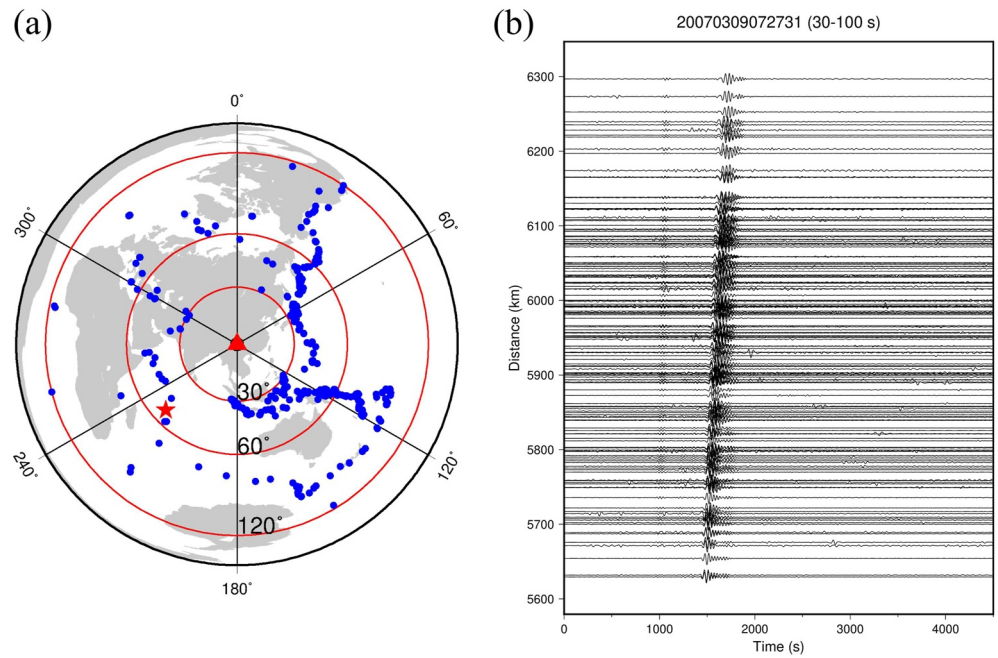

Figure 4. (a) Distribution of earthquakes (blue dots) used for teleseismic two-plane-wave tomography. The red triangle represents the center of stations. (b) Teleseismic waveforms with the source location indicated by the red star in (a).

the selected teleseismic events are measured through the FTAN method, and they are inputted to the TWPT to construct Rayleigh wave phase velocity maps at periods of 30–140 s (Figure 5). Same as the ANT, we parameterize the study region using a 0.25° × 0.25° grid.

To provide a quantitative assessment of resultant phase velocity maps, we conduct a series of checkerboard tests for both ANT and TPWT. We design a checkerboard velocity model with ±8% amplitude anomalies relative to the average phase velocities of resulting phase velocity maps from field data. For ANT, the sizes of the anomalies are set to 0.5° × 0.5° for periods of 8, 20, 30, and 40 s (Figure S2 in Supporting Information S1). For TPWT, the sizes of the anomalies are set to be slightly larger, 1.5° × 1.5° throughout the periods (Figure S3 in Supporting Information S1). The recovered velocity features from our checkerboard resolution tests are summarized in Figure S2 and S3 in Supporting Information S1. In general, the test results show that the input anomalies are recovered well for almost all our study areas thanks to unprecedently dense station coverage. Based on these tests, we are confident that our model resolutions reach ~50 km for most of the crustal part, while the model resolution degrades with depth due to the broadening of the surface wave sensitivities at longer periods. The nearly complete recovery of the 1.5° × 1.5° sized anomalies at the intermediate to long period range (60–120 s) indicate that our model resolution at the lithospheric scale is less than 150 km.

The phase velocities at the overlapping periods between the two tomography methods are very consistent with each other with an average difference smaller than 4%. Figure S4 in Supporting Information S1 shows one example of the difference at 40 s period. Similar to W. Shen et al. (2016), we calculate the weighted average of the Rayleigh wave phase velocities from ANT and TPWT at the overlapping periods of 30–50 s where the weight applied to ANT changes linearly from 1 to 0 with periods. Finally, we obtain 5–140 s Rayleigh wave phase velocity maps and extract local dispersion curves at each station location, which are then combined with station-dependent body-wave waveform data to jointly invert for V_s structures beneath each station.

2.3. Teleseismic Body-Wave Data

When a teleseismic *P* wave encounters the Moho, a *P*-to-*S* conversion is generated at the interface. Due to the nearly vertical incidence of *P* wave, the *Z* component waveforms received at the surface show only apparent direct *P* waves. However, in the *R* component, in addition to the direct *P* wave, it also shows a relatively weak *P*-to-*S* converted wave from the Moho. The same thing happens when a *P* wave encounters the sediment-bedrock boundary, which generates an additional *P*-to-*S* converted wave at the sediment base. With large velocity impendence,

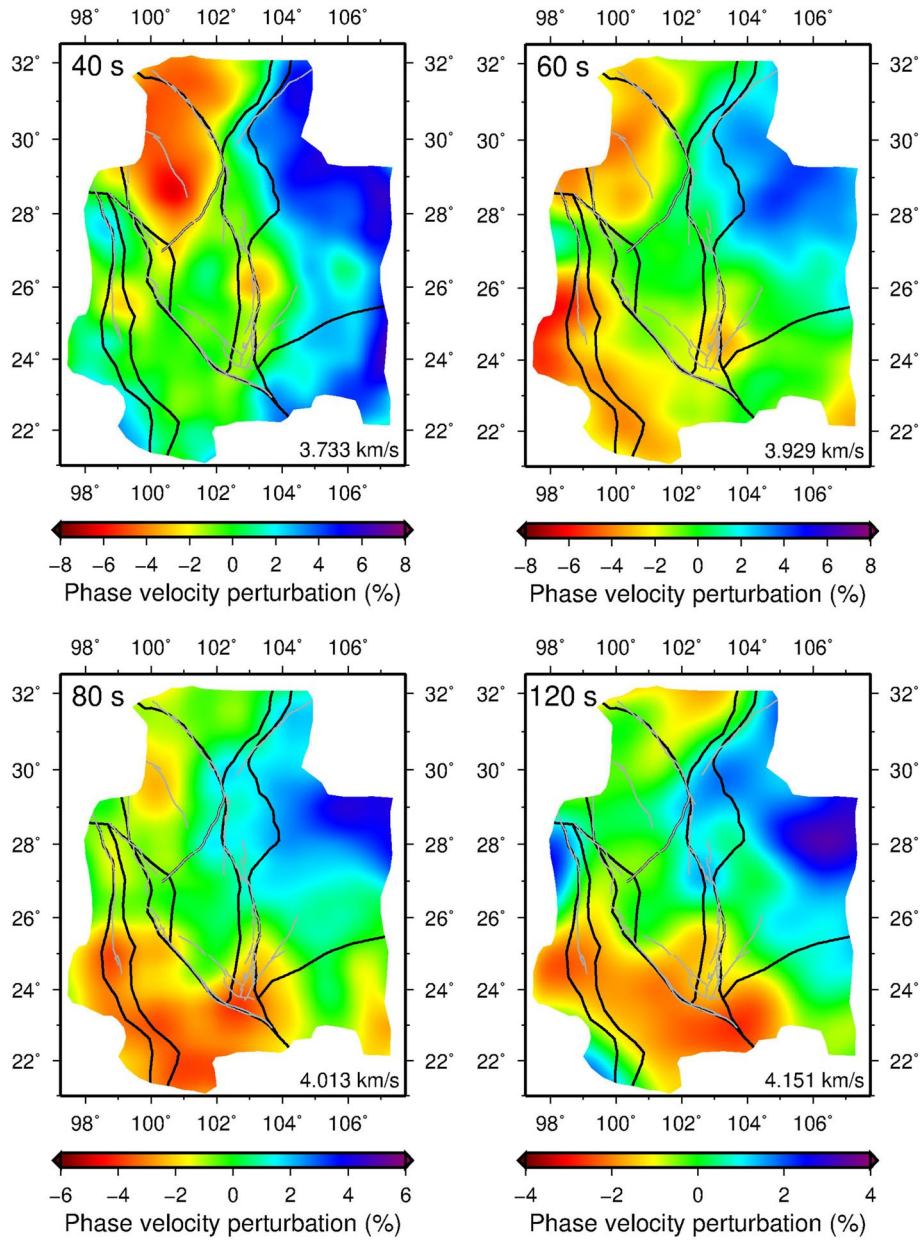

Figure 5. Phase velocity maps at different periods from teleseismic two-plane-wave tomography.

this *P*-to-*S* conversion is strong enough to interfere with the direct *P* wave in the *R* component, delaying the arrival time of apparent *P* wave. The time delays are period-dependent and can be used to invert for the structure of the sedimentary layer (Y. Bao & Niu, 2017). Besides, the multiples from the sedimentary layer of stronger energy can also mask or interference with the *P*-to-*S* conversion from the Moho, making it difficult to separate from each other. To avoid this complexity, in this study, we employ the cross-convolution method (Bodin et al., 2014; G. Li, Niu, et al., 2019; Menke & Levin, 2003) to invert the entire *Z* and *R* component waveforms for the subsurface interfaces and velocity structure. The basic theory relies on the following two equations:

$$Z_{\text{obs}}(t) * r_{\text{pred}}(t, m) = s(t) * z(t) * I(t) * r_{\text{pred}}(t, m) \tag{1}$$

$$R_{\text{obs}}(t) * z_{\text{pred}}(t, m) = s(t) * r(t) * I(t) * z_{\text{pred}}(t, m) \tag{2}$$

where $Z_{\text{obs}}(t)$ and $R_{\text{obs}}(t)$ represent the observed vertical and radial components of teleseismic body waves, $z(t)$ and $r(t)$ are the vertical and radial component Green's functions of the structure below the station, $s(t)$ and $I(t)$ are

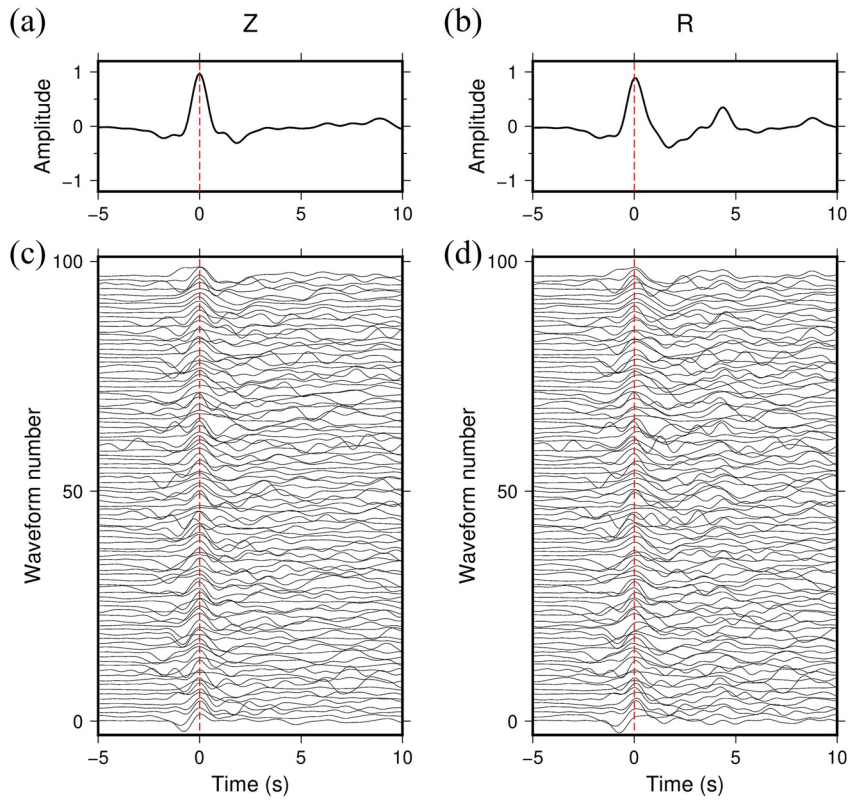

Figure 6. *Z*-component (c) and *R*-component (d) waveforms from all teleseismic events recorded at station X1.53207 with the stacked waveforms shown in (a) and (b), respectively.

the seismic source function and the instrumental response function, and $z_{pred}(t,m)$ and $r_{pred}(t, m)$ are the predicted vertical and radial component Green's functions of the sampled model m. When the sampled model m is the same as the real velocity structure below the station, that is, $z_{pred}(t, m) = z(t)$ and $r_{pred}(t, m) = r(t)$, the two convolution waveforms in the above equation are also equal.

Since the convolution operation is linear and the body wave Green's function of the shallow structure is almost independent of the epicenter distance for teleseismic events between 30° and 90° (G. Li, Niu, et al., 2019), we stack the body-wave waveforms recorded at each station to improve the SNR of the waveforms, which also reduces the number of waveforms to be fitted in the inversion. Following the data processing procedure of G. Li, Niu, et al. (2019) and G. Li et al. (2021), we select 1,180 teleseismic events with $M_s > 5.5$ and epicenter distance of 30°–90° that occurred during the observation period. Based on the source and station locations, we rotate the two horizontal components (E and N) to obtain the *R*-component waveforms. We predict the arrival time of the direct *P* wave based on the AK135 model (Kennett et al., 1995) and then use the maximum amplitude around the predicted arrival of the *Z* component to normalize the *Z* and *R* components simultaneously. If the polarity of the teleseismic *P* wave is negative, we reverse it by multiplying the *Z* and *R* component waveforms with minus one. For events with SNR larger than 10, we align their waveforms according to the moments of maximum amplitudes and then stack them together as illustrated in Figure 6. Here the SNR is defined as the ratio of the maximum amplitude of the body-wave waveform to the root mean square of the noise window, which is 60–10 s before the arrival of the direct *P* wave. Finally, the stacked waveforms with a time spanning of 5 s before and 10 s after the maximum amplitude are used to calculate the misfit function in the joint inversion. Figure 6 shows one example of teleseismic waveforms recorded by station X1.53207, whose location is marked in Figure 1.

2.4. Joint Inversion

Rayleigh wave phase velocities and teleseismic body-wave waveforms have complementary sensitivities to seismic structures and jointly inverting them can reduce the trade-off between absolute S wave velocities and depths

Table 1
Search Ranges of Model Parameters

Model parameters		Search range	Reference model
Sediment thickness		0–12 km	/
V_s at the top of the sediment layer		0–3 km/s	Bassin et al. (2000)
V_s at the bottom of the sediment layer		0–3 km/s	Bassin et al. (2000)
V_p/V_s of the sediment layer		1.8–3	/
Crust thickness		±10 km	W. Wang et al. (2017)
5 B-splines of the crust (1–5)		±15%	FWEA18 model (Tao et al., 2018)
8 B-splines of the upper mantle	(1–5)	±15%	
	(6)	±8%	
	(7–8)	±2%	
Uncertainties (σ_1, σ_2)		10^{-3}–10^{-1}	/

of discontinuities (G. Li, Niu, et al., 2019). In this study, we employ a Markov Chain Monte Carlo inversion method implemented with a delayed rejection and adaptive Metropolis algorithm (Haario et al., 2006) to guide the model selection. We adopt the two-stage strategy of G. Li, Niu, et al. (2019) to sample the model space. In the first burn-in stage, 160,000 models are sampled from the initial search range following a randomly uniform distribution, where the posterior probability distributions of the model parameters are estimated and then used as a prior for the subsequent sampling. In the second stage, a total of 120,000 models are constructed and the posterior probability distribution is updated every 40,000 iterations. Finally, 5,000 independent models are further selected from all accepted models in Markov Chain and those independent models are used to calculate the maximum probability model.

Similar to G. Li, Niu, et al. (2019), the misfit function is defined as

$$M_{\text{joint}}(m) = \frac{1}{\sigma_1^2 N} \sum \left(\frac{PH_{\text{pred}}(m) - PH_{\text{obs}}}{\sigma_{PH}} \right)^2 + \frac{1}{\sigma_2^2} \varphi(m) \tag{3}$$

$$\varphi(m) = 1 - \frac{\int_{T_1}^{T_2} \left\{ Z_{\text{obs}}(t) * r_{\text{pred}}(t,m) \right\} \cdot \left\{ R_{\text{obs}}(t) * z_{\text{pred}}(t,m) \right\}}{\sqrt{\int_{T_1}^{T_2} |Z_{\text{obs}}(t) * r_{\text{pred}}(t,m)|^2 dt} \cdot \sqrt{\int_{T_1}^{T_2} |R_{\text{obs}}(t) * z_{\text{pred}}(t,m)|^2 dt}} \tag{4}$$

where $PH_{\text{pred}}(m)$ represents the predicted phase velocity of the sampled model m, PH_{obs} represents the observed phase velocity, σ_{PH} is the phase velocity uncertainty, N is the number of periods, $\varphi(m)$ is the misfit function of the body-wave waveform, T_1 and T_2 are the time windows of the body-wave waveform, and σ_1 and σ_2 are the uncertainties of the two data sets. Following Bodin et al. (2012), we also take the uncertainties of σ_1 and σ_2 as unknown parameters in our inversion. During the forward calculation, we use the Computer Programs in Seismology (Herrmann, 2013) to calculate Rayleigh wave phase velocities and adopt the propagator matrix method (Haskell, 1962; Thomson, 1950) to synthesize the Green's function of body waves.

Our 1D velocity profile extends from the surface down to 410 km depth below the station and is represented by three major layers, that is, a sedimentary layer, a crustal layer, and a mantle layer. We use four parameters to represent the sediment layer, including the V_s at the top and bottom of the sediment layer, the layer thickness and the associated V_p/V_s ratio. The crustal layer is characterized by six parameters with one for the crustal thickness and five B-spline coefficients modeling the variations of V_s in the crust. We use a total of eight B-splines to describe the V_s structure of the upper mantle extending from the Moho (W. Wang et al., 2017) to 410 km depth. Considering the limited sensitivity of our data to V_s structures at depths beyond 250 km, we reduce the model space for the last three B-splines that are mainly sensitive to V_s at great depths. The detailed model space for all parameters is shown in Table 1. During the inversion, we scale V_p and density from V_s following different empirical relationships depending on the layer type. In the sedimentary layer, V_p is scaled by V_s using the separate parameter of V_p/V_s, and the density is scaled from V_p following the relationship of

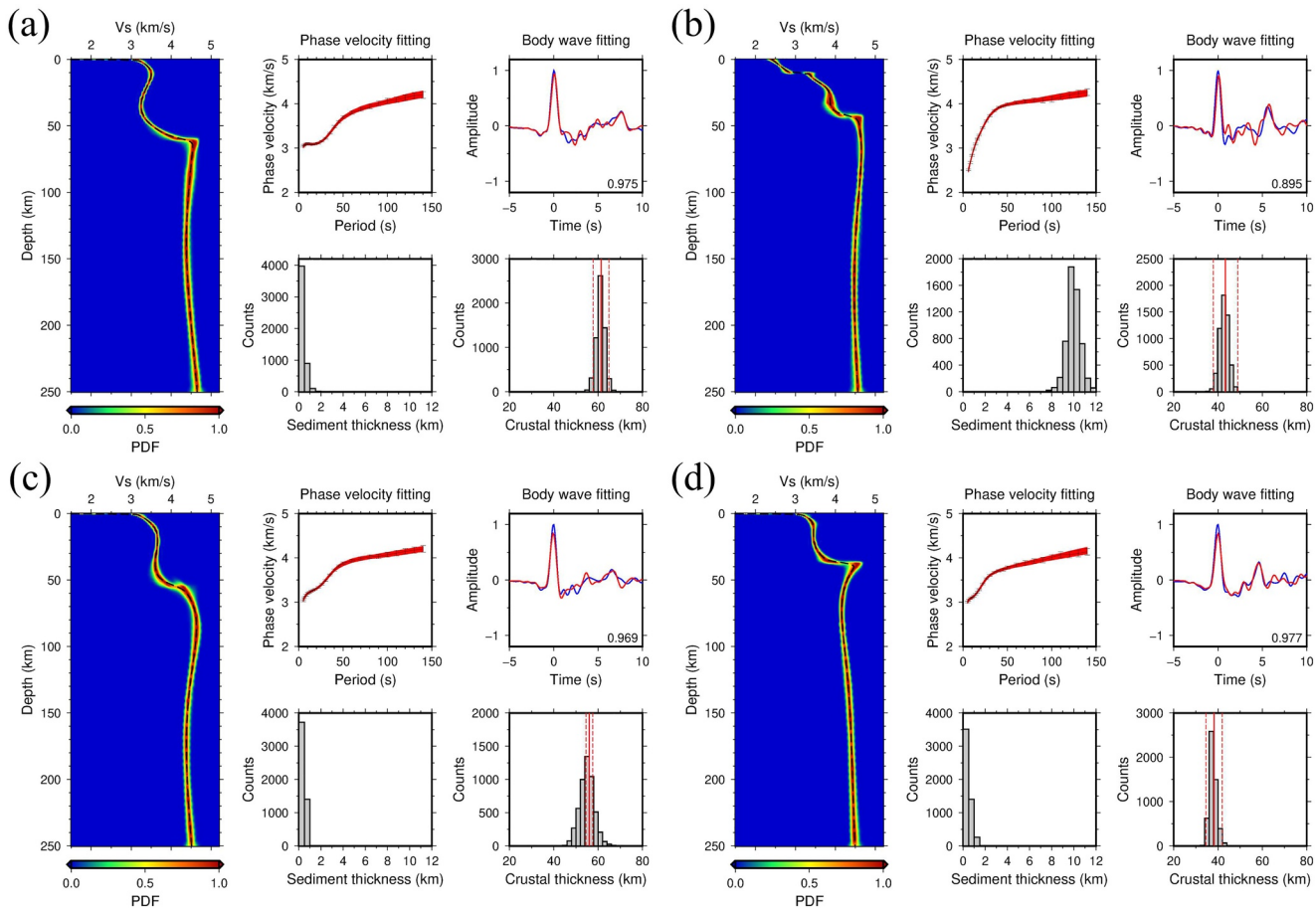

Figure 7. Posterior density function (PDF) of the V_s (black dashed line: the mean of all acceptable models), histograms of sediment and crust thickness (red solid line: the reference value from W. Wang et al. (2017); red dashed lines: the corresponding uncertainty), as well as the fitting of Rayleigh wave phase velocities (error bars: the observed phase velocities; red lines: the theoretical values calculated from all acceptable models) and convolution waveforms (blue line: the cross convolution of $Z_{obs} * r_{pred}$ calculated from the mean model; red line: that of $R_{obs} * z_{pred}$) for four stations located in the North Chuan-Dian Block (a), the Sichuan Basin (b), the Emeishan Large Igneous Province (c), and the Indo-China Block (d).

$\rho = 1.74V_p^{1/4}$ (Gardner et al., 1974). In the crust, V_p and density are scaled from V_s following Brocher's law (Brocher, 2005):

$$V_p = 0.941 + 2.095V_s - 0.821V_s^2 + 0.268V_s^3 - 0.025V_s^4 \quad (5)$$

$$\rho = 1.661V_p - 0.472V_p^2 + 0.067V_p^3 - 0.0043V_p^4 + 0.000106V_p^5 \quad (6)$$

In the upper mantle, at depths shallower than 200 km, we scale V_p to V_s by a constant relationship of $V_p/V_s = 1.79$ following the AK135 model (Kennett et al., 1995) and scale density to V_p using the Birch's law of $\rho = (V_p + 2.4)/3.125$ (Birch, 1961). For depths deeper than 200 km, we scale V_p and density using the derived relationships of $V_p/V_s = 1.85$ and $\rho = 0.327V_p + 0.705$ based on the PREM (Dziewonski & Anderson, 1981).

3. Results

By jointly inverting the phase velocities and teleseismic body waveforms, we obtain the 1D S-wave velocity model from surface down to 410 km depth below each station (Figure 7). We assemble the 1D velocity models beneath all stations to obtain a 3D V_s model for the SET.

The inclusion of teleseismic body-wave waveforms in the inversion improves the constraints on the sediment thickness and Moho depths as demonstrated by the tight *posterior* distributions. However, limited by the smooth

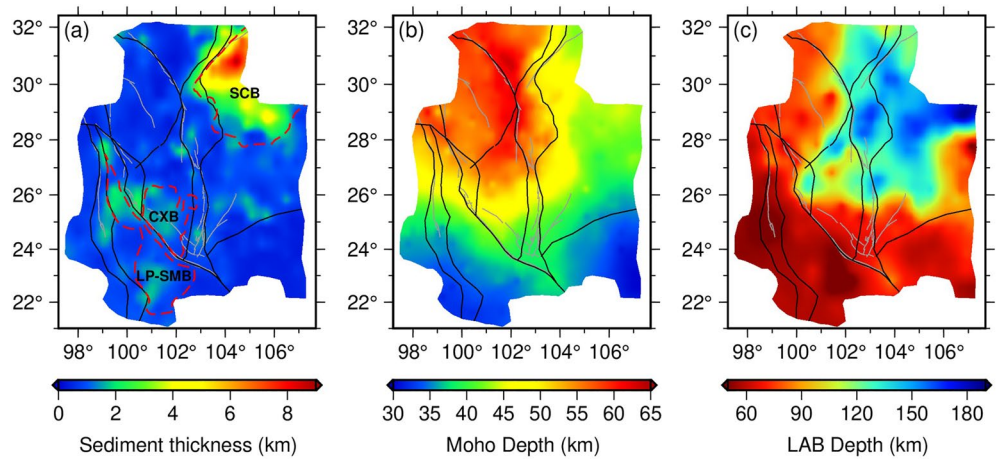

Figure 8. (a) Sediment thickness, (b) Moho depth and (c) lithosphere and asthenosphere boundary depth maps. The red dashed lines delineate the range of main basins.

nature of the B-spline functions, only the arrival and amplitude of main phases in the convolution waveforms can be fitted. Figure 7 shows the inversion results of 1D shear-wave structures beneath four stations located in the NCDB, Sichuan Basin (SCB), ELIP, and Indo-China Block (ICB), respectively. Strong variations of crustal and lithospheric structures can be observed through the four locations. For example, prominent LVZs are observed in the mid-lower crust beneath the station at NCDB (Figure 7a); thick sediments are observed beneath the station at SCB (Figure 7b); a high-velocity upper crust is observed beneath the station at ELIP (Figure 7c); and a significant low-velocity upper mantle (60–80 km) is seen beneath the station at ICB (Figure 7d).

To assess how the inclusion of teleseismic body-wave waveforms improve the inversion result, we conduct another set of 1D inversion solely using Rayleigh wave phase velocity data. The inversion results for the same points shown in Figure 7 are summarized in Figure S5 in Supporting Information S1. In general, the resultant 1D models from the new inversion are very similar to those from the joint inversion at the lithospheric scale. However, significant differences exist on the discontinuity depths, such as sedimentary thickness and Moho depth, with a much larger and sometimes biased probability distributions for those without using teleseismic body-wave waveforms. For example, the new result from a point at NCDB region (Figure S5a in Supporting Information S1) shows a mean Moho depth of 57 km, which is much shallower compared to those from the joint inversion and from the receiver function result (~62 km) in the region. Another point at the SCB (Figure S5b in Supporting Information S1) shows that the sediment thickness is totally underestimated (only 2–3 km) in the new inversion where our joint inversion gives a value of ~10 km that is more consistent with the sonic well log data (M. Wang et al., 2016). The differences in the interface depth also results in slight changes of V_s above/below these depths due to the tradeoffs between the isotropic parameters and discontinuity depths. Including teleseismic body-wave waveforms helps reduce this tradeoff.

In addition, we also calculate the vertical gradients of the V_s models in the upper mantle and approximate the depth of the maximum negative gradient as the lithosphere and asthenosphere boundary (LAB) (Figure S6 in Supporting Information S1). To retrieve the sediment thickness, the Moho depth and LAB, we further perform the interpolation-based inversion method of Niu et al. (2007) to get smoother interfaces from all measurements. The details of this method are described in Appendix A. Figure 8 summaries the regional variations of sediment thickness, Moho depth and LAB from this study. We also extract several horizontal slices at different depths and vertical cross sections through the main geological units to show the main features of our 3D model (Figures 9 and 10).

At 5–10 km depth of the upper crust (Figures 9a and 9b), low velocity anomalies are observed beneath various sedimentary basins, such as SCB and Lanping-Simao Basin (LP-SMB), as well as along the major fault zones, such as the LXF, the XJF, the Chuxiong-Tonghai Fault, the Mule-Shizong Fault, and the Nujiang Fault. Interestingly, the SCB tends to be separated into two distinct domains with the northern SCB characterized by more significant velocity reductions compared to the southern one. This difference corresponds to a thicker sedimentary layer, up to 9 km, in the north compared to a ~4 km sedimentary layer in the south. Our model (Figure 8a)

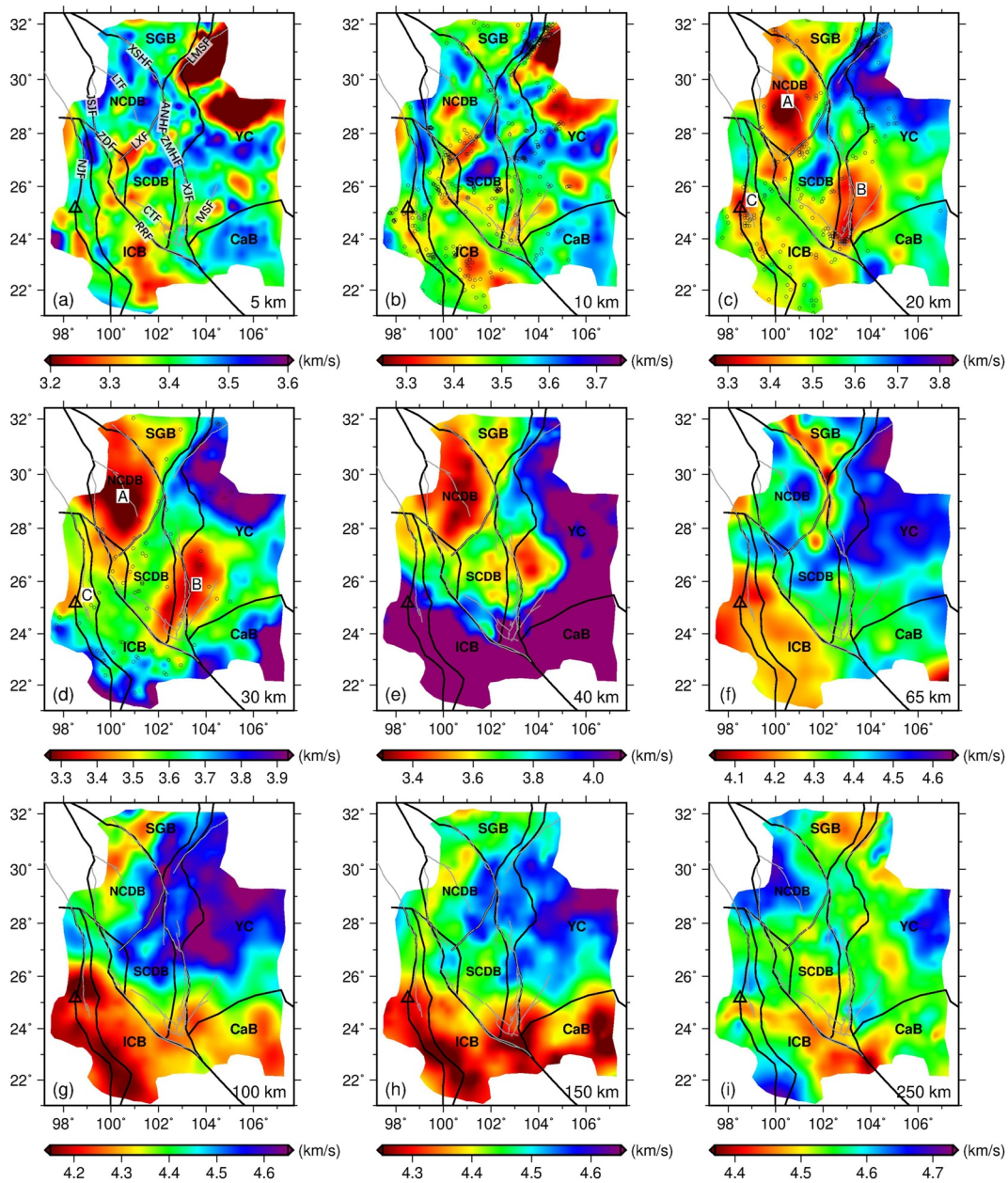

Figure 9. V_s maps at different depths. The triangle denotes the Tengchong volcano zone. The black circles in (b)–(d) represent the locations of earthquakes with $M_s > 4.0$ occurred from 1970 to 2017.

also reveals 2–3 km thick sediments in the LP-SMB, the Chuxiong Basin (CXB), and some other smaller-scale basins. At such depths, high velocity anomalies are mainly distributed in the mountain ranges around the SCB, the Youjiang fold zone of the Cathaysia Block (CaB), the northern portion of the NCDB, and the inner zone of the ELIP in the South Chuan-Dian Block (SCDB).

At the middle and lower crust of 20–30 km depth (Figures 9c and 9d), the major velocity features are three disconnected LVZs located in the NCDB (A), the XJF and its eastern region (B), and the Tengchong volcanic zone (C), respectively. In particular, anomalies A and B are well separated by NE-SW trending high velocities, which extend all the way from the eastern SCB, cross the Anninghe Fault (ANHF) and terminate at the SCDB. The vertical cross sections in Figure 10 show the 3D distribution of the above-described features more clearly. Anomaly A exhibits the most significant velocity reductions in the crust (with absolute $V_s < 3.3$ km/s) and extends vertically at 10–45 km depths (profiles OA, OB, OC, and OD). This anomaly becomes less prominent when extending southward across

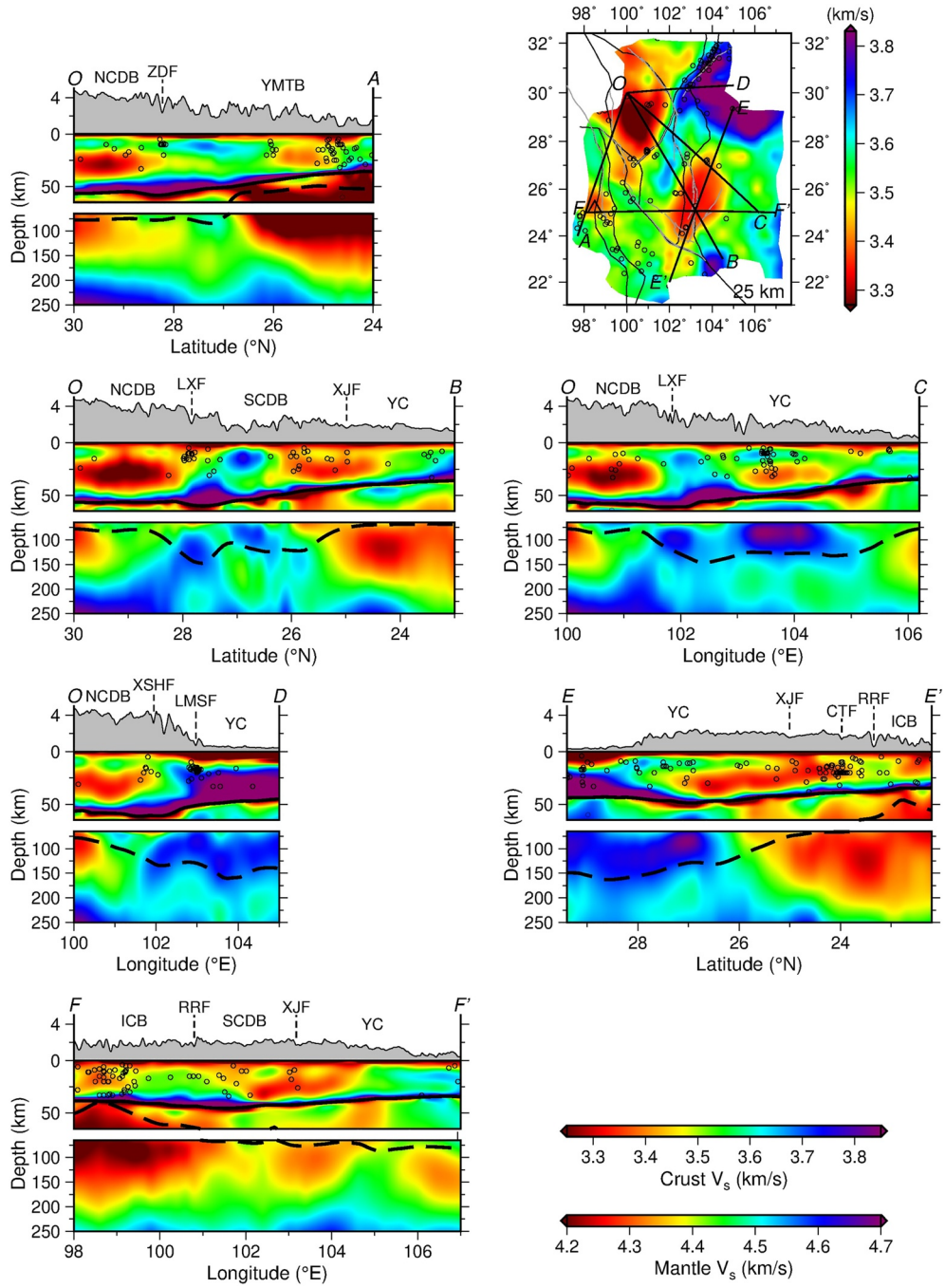

Figure 10. Vertical profiles (OA-OD, EE', and FF') of our V_s model with their locations displayed in the plain maps of 25 km depth on the top right. The vertical exaggeration of 0–65 km depth is 2.29 and that of 65–250 km depth is 1.07. The black circles represent the locations of earthquakes with $M_s > 4.0$ occurred from 1970 to 2017. The black dashed lines indicate the lithosphere and asthenosphere boundary along profiles.

the Zhongdian Fault (ZDF), but it clearly terminates before reaching the Tengchong volcano (profile OA). To the east and southeast, the anomaly A is confined by the LXF and the Longmenshan Fault (LMSF), respectively, likely due to the obstruction of the high-velocity blocks at YC and the ELIP (profiles OB, OC, and OD). Compared to the relatively consistent depth range of the anomaly A, Profile EE' shows that the anomaly B exhibits obvious north-south variations. In the north, the crust is thicker, and the LVZ is located at a deeper depth (below 25 km); while in the south, they are much shallower and are accompanied by more earthquakes at the southern edge.

The velocity features at 40 km depth (Figure 9e) mostly reflect the variations of crustal thickness in the region (Figure 8b). At such depth, a broad region of low velocity (<4 km/s) is observed in the northwestern portion of the study area, representing the thicker crust compared to the surrounding regions. At 65 km depth in the uppermost mantle (Figure 9f), the Tengchong volcanic zone and the ICB exhibit concentrated low velocities, while most of the northern YC and the SCDB show high velocities (>4.55 km/s). A narrow zone of concentrated low velocity is also observed along the XSHF, likely indicating its extension to the lithospheric scale. Our restoring resolution test indicates that the narrow low-velocity anomaly along the XSHF at this depth can be well recovered. More details about this resolution test are included in Supporting Information (Text S1 and Figure S7 in Supporting Information S1).

Blow 65 km depth, the Tengchong volcanic zone shows the most significant velocity reduction across the region, and this low velocity seems to extend vertically to ∼100 km depth. At greater depths of 100–150 km (Figures 9g and 9h), a broad low velocity anomaly starts to emerge at regions south of 26°N with sporadic concentrated low velocities beneath the ICB and the CaB (profiles EE' and FF'); while high velocity anomalies beneath the SCDB and the northern YC persist. These high velocities probably represent a thicker lithosphere in the region with estimated LAB depths at ∼150 km (profiles OB, OC, OD, and EE'), compared to a much thinner lithosphere (∼50 km) in the surrounding regions. However, significant high-velocity bodies tend to emerge beneath the Songpan-Ganzi Block (SGB) and the NCDB at depths >200 km (profiles OA, OB, OC, and OD), where our model resolution starts to deteriorate. To better show the relationship of the upper mantle features of our model with the deeper structures, we combine our velocity model covering 0–410 km depths with the full waveform inversion results of Tao et al. (2018) at 410–800 km depth range (Figure 11). This combined model reveals that the location of significant high velocities in the mantle transition zone (MTZ) coincides well with the upper mantle LVZs.

4. Discussion

4.1. Comparison With Previous Models

The eastern and southeastern margins of the Tibetan plateau have received numerous attentions from seismologists to characterize the underlying shear-wave velocity structures as well as the variations of sediment and crustal thickness (e.g., X. Bao, Sun, et al., 2015; M. Chen et al., 2014; Fu et al., 2017; Z. Huang et al., 2019; H. Li et al., 2009; M. Li et al., 2016; Q. Y. Liu et al., 2014; W. Shen et al., 2016; Y. Yang et al., 2012; Y. Yang et al., 2020; Yao et al., 2008; Z. Zhang et al., 2020). In general, our model exhibits similar first-order features to these existing models, such as the thick sedimentary layer in the SCB, extensive LVZs in the middle and lower crust of the NCDB and along the XJF, the high-velocity crust beneath YC, and significant low-velocity in the upper mantle beneath the ICB and the CaB. However, the inclusion of 653 stations from two dense arrays and the use of advanced joint inversion of broad period ranges of dispersion and body wave data result in unprecedented resolution of our new model, which reveals remarkable small-scale features that are not observed clearly in previous studies.

Since our model covers a broad depth range extending from the surface down to >250 km, we compare our model with others at two separate domains: the crust and the upper mantle depth, respectively. To better facilitate the model comparison, we obtain the digital form of several recently published models and replotted them on the same grid points using the same color scales (Figure 12 and Figure S8 in Supporting Information S1).

We first compare our crustal features with those of Y. Yang et al. (2020) and Y. Liu, Yao, et al. (2021) (Figure 12). Both models are recently published and focus on the crustal structures of SET through joint inversion of multiple datasets, but are constructed using different data sizes and types. For example, Y. Yang et al. (2020) use surface wave data (dispersion and H/V ratio) and *P* wave receiver function from 114 (permanent) stations in the region; while Y. Liu, Yao, et al. (2021) use surface wave dispersion data from 175 stations (124/175 are permanent stations) and body wave traveltime data of local earthquakes from 230 (permanent) stations. The least number of stations used in Y. Yang et al. (2020) among the three studies result in the smoothest features of their model in the shallow crust, where Y. Yang et al. (2020) also show several anomalies different from the other two (10 km depth in Figure 12). For example, broad high velocities are observed on the eastern side of the ANHF and Zemuhe Fault (ZMHF), the ICB, and the southern YC, where finer-scale and more localized variations of velocities are revealed in the other two models. Y. Liu, Yao, et al. (2021) resolve small-scale features at a level similar to ours, though some discrepancies exist at local regions. For example, their model shows broad low velocities

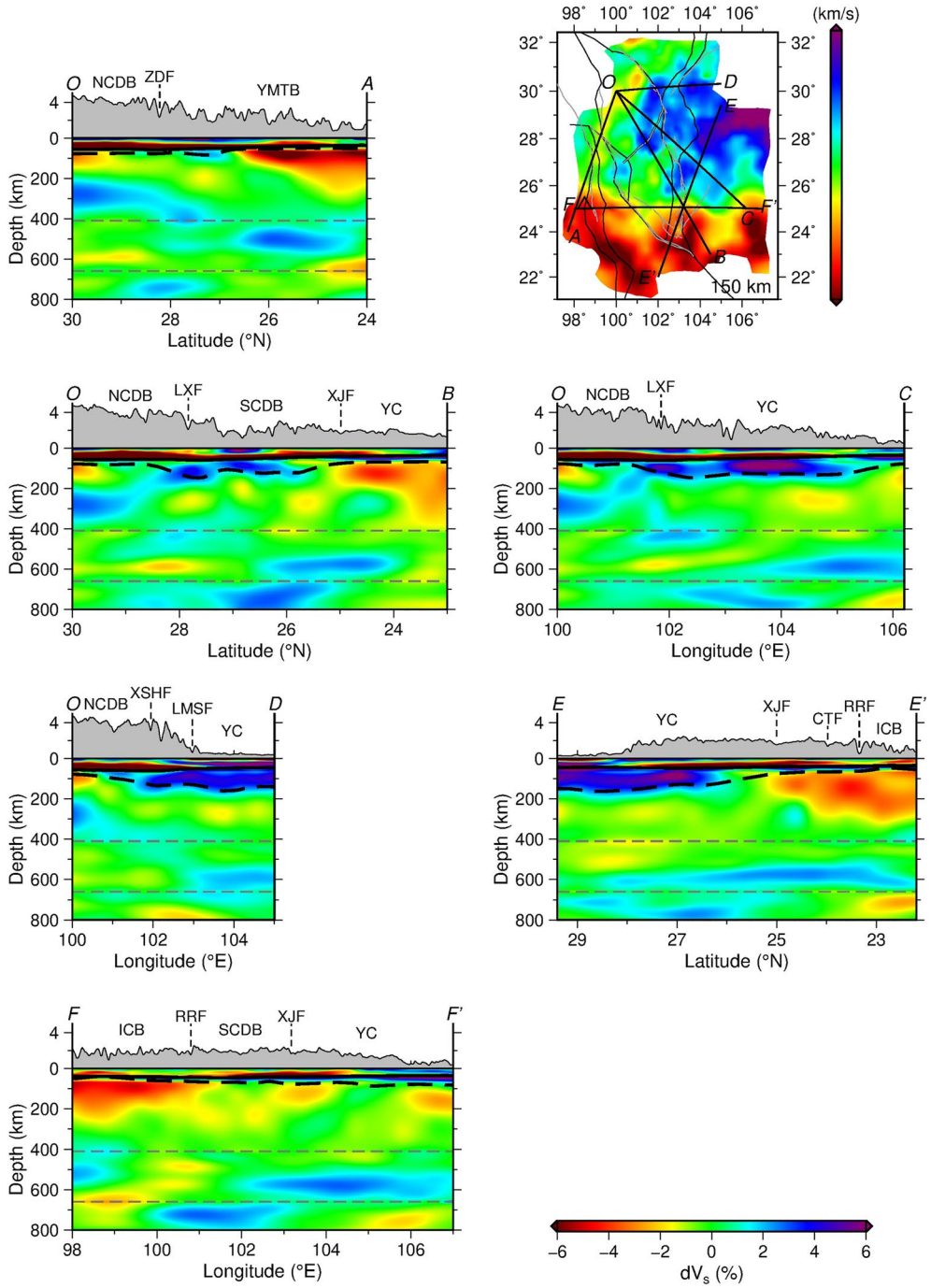

Figure 11. Same as Figure 10, but velocity perturbation profiles at 0–800 km depth with 0.48 of vertical exaggeration.

in the NCDB, while our model suggests that the low velocities are only concentrated in a local area northwest of the LXF. In addition, their model shows significant low velocities in the CaB, which is the opposite in our model. These regions of large discrepancy have generally sparser station coverage in Y. Liu, Yao, et al. (2021), thus the related features may be not well resolved as demonstrated in their resolution tests. In the upper crust, another major difference of the models lies in the resolved sediment thickness in the SCB. Our model delineates a deeper basin structure (taking ~2.7 km/s as the approximate bottom boundary) with up to 9 km sediments in the northern SCB, compared to the thinner (~4–5 km) sporadic subbasins in the south (Figure 8). This feature is consistent with the sonic logs and seismic reflection profile results in the region (C. Y. Wang, Wu, et al., 2003; M. Wang

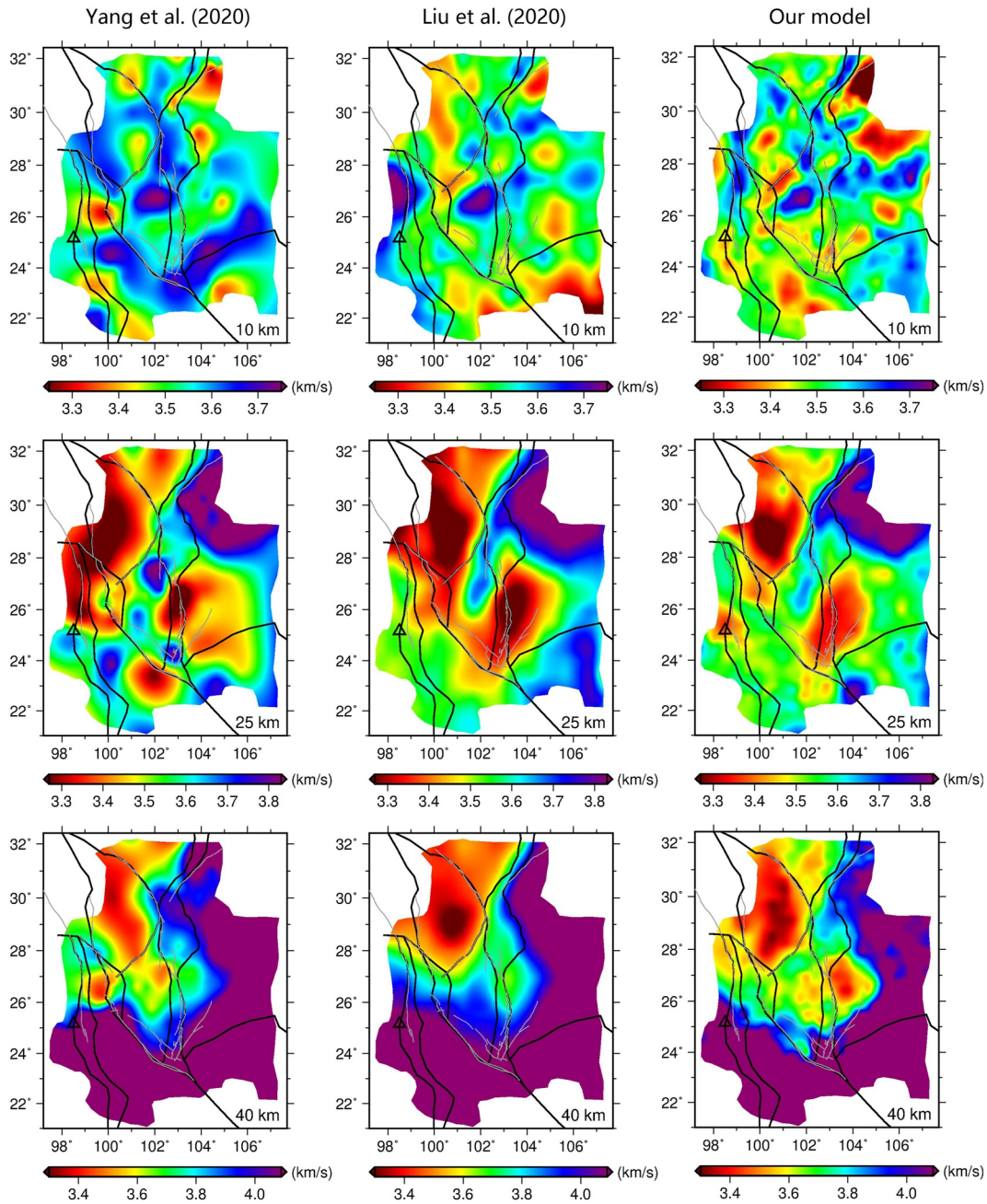

Figure 12. Comparisons of our model (right column) with that of Y. Yang et al. (2020) (left column) and Y. Liu, Yao, et al. (2021) (middle column) in the crust depth.

et al., 2016). Meanwhile, significant high velocities (~3.4 km/s at 5 km depth) are observed in the central SCB beneath the thin sediments, corresponding well with the contractional anticlines having a high-velocity core of Precambrian metasedimentary and igneous rocks (M. Wang et al., 2016). However, Y. Yang et al. (2020) observes a smoother sedimentary basin with a broad thickness of ~6–8 km, and Y. Liu, Yao, et al. (2021) does not resolve the sedimentary structure well due to the weak sensitivity of their data to the sedimentary layer.

The most pronounced differences of the three models appear in the mid-lower crust, where the distribution and connectivity of LVZs show strong variations (25 km depth in Figure 12). For example, Y. Yang et al. (2020) and Y. Liu, Yao, et al. (2021) as well as many other previous studies (e.g., X. Bao, Sun, et al., 2015; Z. Zhang et al., 2020) all observe a laterally continuous LVZ extending from the NCDB to the Tengchong volcano, while

our model reveals two separated LVZs in the region. We further describe this feature and discuss its related implication in Section 4.2.

Next, we compare the upper mantle part of our model with those of W. Shen et al. (2016) and Z. Zhang et al. (2020) (Figure S8 in Supporting Information S1), who use similar period ranges of surface wave data as our study obtained from both ANT and teleseismic surface wave tomography. Compared to that in the crust, the velocity variations in the upper mantle are much smaller between the models. One of the main differences in the velocity features lies beneath the SCDB, where only our model shows local high velocities at the top of the upper mantle (above 110 km depth). However, a similar high-velocity anomaly is observed in the teleseismic body wave tomography model incorporating the same dense array in the region (Z. Huang et al., 2019). In addition, although all three models reveal some localized velocity reductions around the XSHF, our model delineates a LVZ more closely following the fault trend, suggesting its extension to the lithospheric scale (70 km depth in Figure S8 in Supporting Information S1). Compared to the other two models, our model shows more significant velocity reductions in the upper mantle beneath the NCDB and the SGB, which is consistent with the recent body wave tomography of Z. Huang et al. (2019). The three models exhibit considerable variations of velocity features beneath the Tengchong volcanic zone as well as the broad region south of 26°N, which are discussed further in Section 4.4.

4.2. Spatial Distribution of Crustal LVZs

A variety of geophysical observations suggest the existence of low viscous materials in the mid-lower crust of the SET. These geophysical features include particularly low shear-wave velocity (<3.4 km/s) (X. Bao, Sun, et al., 2015; Y. Yang et al., 2020; Yao et al., 2008; Z. Zhang et al., 2020), abnormally high electrical conductivity (Bai et al., 2010; X. Li et al., 2020), high heat flow (Hu et al., 2000), and strong attenuation (L.-F. Zhao et al., 2013). With the use of even more and denser data, our new model exhibits higher resolution across the broad area and reveals three independent low-velocity regions (A, B, and C) in the middle-lower crust of the SET (Figures 9c and 9d).

Anomaly A is one of the major features in the mid-lower crust depth of our model, which has been observed in many previous seismic models (e.g., X. Bao, Sun, et al., 2015; Z. Zhang et al., 2020). However, compared to previous studies, our model shows more enhanced velocity reductions at 20–40 km depths with the absolute V_s at the core region lower than 3.25 km/s. In addition, our model shows that this anomaly is clearly confined by the large-scale fault systems of LXF and LMSF (P. Z. Zhang, 2013) to the southeast and east. Y. Yang et al. (2012) argues that an absolute V_s below 3.4 km/s at such depths is very difficult to explain without the presence of melts. Supported by other geophysical signatures described above, this LVZ is often interpreted as a mechanically weak layer that could flow in a geological time scale. However, since these geophysical models only represent the current in situ measurements, and the crust beneath this region is thick today (Figure 8b), it is difficult to infer whether this LVZ is formed from crustal thickening due to other reasons, for example, radiogenic heating from early growth after the Indian-Tibetan plate collision (McKenzie & Priestley, 2008), or a result of channelized flow that has thickened or is thickening (parts of) the crust.

Seismic anisotropic signatures (H. Chen et al., 2016; H. Huang et al., 2010; Y. Liu, Li, et al., 2021; Sun et al., 2012; Xie et al., 2013, 2017; Yao et al., 2010), whose formation is directly linked to past deformation, show azimuthal anisotropy of fast axes sub-parallel to the strikes of the LVZ and strong positive radial anisotropy at the depths corresponding to the LVZ. The anisotropy is interpreted as a result of horizontal flow of a mechanically weak layer with mica-bearing compositions. In this case, the anomaly A could represent a remanent of previous channels that could be still active. Indeed, large scale V_s models covering the entire eastern Tibetan Plateau (Y. Yang et al., 2012; Yao et al., 2010) reveal several LVZs of similar amplitude in the central Tibetan Plateau, with which the anomaly A seems to be weakly connected, suggesting its possible initiation from the central Tibetan Plateau. More recently, the high-resolution azimuthal anisotropy model from X. Bao et al. (2020) observes weak azimuthal anisotropy around the anomaly A, and they argue that this channel flow might be strong but have to be disordered to form the relatively weak anisotropy averaged at ∼200 km scales. This could be the case considering crustal thickening process might be heterogenous and achieved soon after the Indo-Asian collision based on paleoaltimetry studies (e.g., S. Li et al., 2015). However, the weak azimuthal anisotropy could still be a result of channelized flow in the mid crust, where mica-bearing rocks (of hexagonal geometry) align horizontally due to the shearing and form strong radial anisotropy but weak azimuthal anisotropy simultaneously. In any case, the

local crustal LVZ we imaged around the NCDB could still be transported to the surrounding topographic lows driven by lateral gravity gradient.

The confinement of anomaly A by the several large-scale strike-slip faults is a very interesting feature. GPS measurements indicate significant sinistral shortening occurring along the LXF on the surface (Hao et al., 2016; P. Z. Zhang, 2013), suggesting strong localized deformation (X. Bao et al., 2020; Q. Y. Liu et al., 2014). The LAB variations and V_s model derived from our model suggest relatively fast and thick lithosphere to east of the LXF. In particular, the high velocity anomaly beneath the inner ELIP is associated with high Poisson's ratio, strong negative radial anisotropy, and high density, which are all interpreted to be related to the upwelling and underplating of the mantle plume (Y. Chen et al., 2015; Y. Deng et al., 2016; Y. Liu, Li, et al., 2021; W. Wang et al., 2017; Y. Yang et al., 2020). And the weak azimuthal anisotropy within the inner ELIP suggests that it is less deformed by the compression of the Tibetan Plateau and may act as a rigid barrier to the southeastward flow of crustal low-viscous materials from the plateau (Han et al., 2022; Z. Huang et al., 2018). In this case, the strong convergence at the shallow crust might decouple the mid-lower crust with the lithospheric mantle, creating shear heating that further enhance the LVZs, as suggested by Q. Y. Liu et al. (2014). X. Bao et al. (2020) propose that the shear heating due to strike-slip faulting along the Litang fault could also contribute to this LVZ. However, this effect might be minor considering the LVZ extending to a much broader region beyond the extent of the fault.

To the south of the anomaly A, we observe a much thinner, less prominent and finger-like low velocity feature, which extends across the ZDF and penetrates into the mid crust of the neighboring block (profile OA in Figure 10). This feature might represent the current active crustal flow initiated from the anomaly A, driven by the positive topographic gradient from north to the south. This interpretation is further consistent with the N-S anisotropic fast-axis orientation in the southern part of the NCDB (X. Bao et al., 2020; Han et al., 2020). In summary, we think the current anomaly A probably represents a remanent or still active channelized flow that could have been initiated from the central Tibetan Plateau, which have helped thicken the crust in the region. The strong shortening along the LXF on the shallow crust decouples the mid-lower crust and creates shear heating during this time, further enhancing the LVZ. Driving by the topographic gradient, this LVZ continues to flow southward, beyond the ZDF, representing the latest episode of crustal flow in the region.

After crossing the ZDF, anomaly A extends slightly further to the south with diminished velocity reduction and terminates well before reaching the front of the Tengchong volcanic zone (anomaly C). This novel feature is different from previous studies (e.g., X. Bao, Sun, et al., 2015; Y. Liu, Yao, et al., 2021; Y. Yang et al., 2020; Z. Zhang et al., 2020) that observe continuous low velocity extending all the way from the NCDB to the Tengchong volcanic zone. It means that the extrusion of low-viscous material from the high altitudes of the plateau is very limited and that there may not be widespread crustal flow in the southeastern Tibetan Plateau. Even though this feature is on the edge of the study area, the many stations located around it provide extremely dense ray coverage across the region (Figure S1 in Supporting Information S1) and the checkerboard resolution tests for ANT at periods of 8–30 s show that anomalies smaller than $0.5° \times 0.5°$ in size can be well recovered in this edge region (Figure S2 in Supporting Information S1), further demonstrating the reliability of this feature. The isolated crustal LVZ of C, mostly beneath the Tengchong volcanic zone, likely indicates a separate magma reservoir in the mid-lower crust that could be sourced from the deeper reservoir in the top of upper mantle (Y. Zhao et al., 2021), where significant velocity reductions present in our model. Both petrological and geochemical signatures of volcanic rocks and melt inclusions around the Tengchong volcano indicate their origin from melting of an enriched mantle (F. Chen et al., 2002; Duan et al., 2019; Zhou et al., 2012). In addition, hydrothermal fluids collected around the Tengchong volcano show high $^3He/^4He$ values, which signatures indicate deeply sourced mantle volatile emissions (M. Zhang et al., 2021).

4.3. A Separated LVZ Beneath the XJF

Apart from the separated LVZs beneath the NCDB and Tengchong volcano, we also observe an isolated LVZ further east of SET beneath the XJF region. This anomaly B has been imaged in many previous studies (e.g., X. Bao, Sun, et al., 2015; Qiao et al., 2018; Z. Zhang et al., 2020). However, different models have led to different interpretations on the origin of this LVZ. For example, X. Bao, Sun, et al. (2015) observe that anomaly B turns southwest after crossing the RRF, which is consistent with the clockwise rotation of crustal motion around the EHS. They further propose its origin from the combined effects of crustal flow and strike-slip faulting in the region. Qiao et al. (2018) and Z. Zhang et al. (2020) showed that the crustal LVZ spreads from north to south and

extends across the RRF into northern Vietnam. Considering the late Paleogene alkaline magmatism and many active faults in Yunnan and northern Vietnam, they suggest that it probably originates from shear heating due to strike-slip faulting or upwelling of the asthenosphere. However, the NE-SW anisotropic fast-axis orientation revealed by the recent azimuthal anisotropy study suggests that the deformation of this LVZ may be related to the southeastward plateau expansion (Han et al., 2022). They propose that tectonic stress from the Tibetan Plateau extrusion has been transferred to the area near the XJF through the SCDB, leading to horizontal crustal shortening and thickening under the NW-SE compression. The ongoing NE-SW surface uplift in the region is supported by GPS measurements (Pan & Shen, 2017). Our new high-resolution results provide further support to this speculation. First, different from past imaging results, our model shows that the anomaly B does not cross the RRF, but is instead confined by the CaB, the ICB and the high-velocity block in the inner zone of the ELIP. Second, the overall NE-SW trend of this LVZ is inconsistent with the N-S trend of the XJF, especially in its northern part, where the LVZ is mainly located east of the XJF. The low Poisson's ratio in the region suggests that the crust may be dominated by felsic materials, which is more susceptible to partial melting from radioactive self-heating (Beaumont et al., 2004; L. Chen et al., 2019; McKenzie & Priestley, 2008), once a thickened crust is formed from the shortening (W. Wang et al., 2017; Z. Zhang et al., 2020).

Our model reveals several other interesting and new characteristics regarding the anomaly B. First, our model indicates the northern portion of the LVZ appears at slightly deeper depths (profile EE' in Figure 10). The significantly thick lithosphere beneath the northern portion of anomaly B probably excludes its origin from local upper mantle upwelling. Instead, the deeper crust might create a local condition of higher temperature, favorable for the in situ partial melting. In the southern part of the LVZ, the low velocities occur at a distinguishable shallower depth (Figure 9b; profile EE' in Figure 10). Our model also shows significant low-velocity anomalies in the uppermost mantle as well as a thin lithosphere, consistent with most previous surface wave imaging studies (e.g., X. Bao, Song, & Li, 2015; W. Shen et al., 2016; Z. Zhang et al., 2020). This suggests the possible existence of crust-mantle material interactions. Y. Zhao et al. (2020) suggest that the origin of this LVZ is related to the localized mantle upwelling. The recent magnetotulleric sounding in the region also suggests that thermal fluids from the mantle may be upwelling along deep faults (X. Li, Bai, et al., 2019). Our model further shows that the south part of the XJF may be the main channel for the upwelling of mantle material to the crust (profile EE' in Figure 10), making it indeed a possible origin of the crustal LVZ. On the other hand, the mantle upwelling might only provide the heat source required for crustal weakening, making it occur at shallower mid-crust depths compared to the northern portion. In addition, we notice significant changes in crustal thickness between the northern and southern sides of this LVZ (B), reducing from 50 km in the north to 40 km in the south (Figure 8b). A similar feature has been observed in some receiver function studies that focus more on Moho variations of the region (e.g., W. Wang et al., 2017). Meanwhile, the paleoaltimetry study reveals the late Miocene surface uplift at the southern XJF (S. Li et al., 2015). The thinner crust and surface uplift in the south may be related to the asthenosphere upwelling in the late Miocene, which is associated with subduction and retreat of the Indian plate (e.g., X. Bao et al., 2020; Richards et al., 2007).

We note a series of earthquakes are concentrated in the southern part of the LVZ and are mainly located along fault zones. The development of low-viscosity material may facilitate the strike-slip of faults and help to release the stress, thus contributing to the occurrence of earthquake clusters around the LVZs in the region. The low-viscosity material may also migrate upward along the local fault system, as revealed by the geomagnetic results of X. Li, Bai, et al. (2019). Meanwhile, the shear heating produced by the strike-slip faulting may also contribute to the formation of the LVZ (X. Bao et al., 2020; Leloup et al., 1999).

Therefore, we attribute the anomaly B mainly to partial melting caused by crustal thickening during the plateau expansion, while its different geometry in the southern part may be a combined result of crustal thickening, mantle upwelling, and shear heating of strike-slip faults.

4.4. Origin of Upper Mantle Upwelling

Previous studies have identified large-scale low-velocity anomalies in the upper mantle over the broad SET region. However, the origin of the low velocity anomalies is still controversial with potential mechanisms including the extrusion of asthenosphere from the Tibetan Plateau (Z. Huang et al., 2015; Z. Huang et al., 2019), dehydration of the subducted Indian plate (Lei & Zhao, 2016; Lei et al., 2019), mantle upwelling associated with plate breakup (Tian et al., 2018; R. Zhang, Wu, et al., 2017), and the delamination of thickened lithosphere caused by the India-Eurasia collision (Feng et al., 2022; Z. Huang et al., 2019). Our new seismic models combined with

other geophysical and geochemical data provide new insights into exploring the origin of the upper mantle LVZs beneath the SET.

In our model (Figures 9f–9h), the upper mantle of the NCDB and the SGB (in the northwestern part of our study area) at depths shallower than 150 km exhibit sporadic low velocities of moderate amplitude (~4.3 km/s). This contrasts with previous body wave tomography results showing widespread low velocities (−2%) around the YC (e.g., Z. Huang et al., 2015; Lei & Zhao, 2016), which are interpreted as extruded asthenosphere material from the Tibetan Plateau. Interestingly, our model shows a significant high-velocity body at 200–250 km depth right beneath the low velocity (profile OA, OB, OC, and OD in Figure 10), and a similar high velocity feature is also observed in the previous body wave tomography of Z. Huang et al. (2019). They interpret this high velocity anomaly as the delaminated lithosphere, which could have induced a potentially localized mantle upwelling (Houseman et al., 1981; Schott & Schmeling, 1998), contributing to the sporadic low velocities in the upper mantle observed in our model. Assuming this delamination explanation is true, we try to estimate its initiation time. Due to the lack of direct constraints on the sinking rate of cold lithosphere in the upper mantle, we use indirect constraints for the region. For the lower bound, we use the average sinking rate of the delaminated continental lithosphere below the MTZ for this region (~2 cm/yr; Feng et al., 2022) considering the much larger viscosity of the lower mantle compared to the upper mantle. For the upper bound, we use the free sinking rate of the oceanic slab in the upper mantle (~3–5 cm/yr; Hafkenscheid et al., 2006; Replumaz et al., 2004), since oceanic slabs typically have higher density than the continental lithosphere. This gives us a range of 2–3 cm/yr for the sinking rate of the cold lithosphere in the upper mantle, which indicates a time span of ~6–10 Myr for ~200 km downwelling on the first order. We note this rough time estimate coincident with the initiation of the activity of XSHF at ~9 Ma ago (Y. Z. Zhang, Replumaz, et al., 2017). Previous studies suggest compressional thickening of the lithosphere and subsequent delamination may lead to the activation of strike-slip faults (Feng et al., 2022; W. Wang et al., 2021), which is consistent with our speculation.

Several lines of evidence exist to support the lithospheric thickening and delamination process in the region after the Indo-Asian collision. First, palaeoaltimetric studies suggest that the eastern plateau reached its approximate current elevation by the late Eocene (Hoke et al., 2014; S. Li et al., 2015), when the lithosphere of the Tibetan Plateau may have thickened significantly. Second, the estimated lithospheric delamination time corresponds well to a change in the Indo-Asian convergence angle (Feng et al., 2022). Based on a plate motion reconstruction model from T.-Y. Lee and Lawver (1995), a notable shift in the convergence direction switching from ~N30°E to below ~N20°E occurs at ~10 Ma. This change of subduction angle may be related to the decrease of resistant force of the eastern plateau after the lithospheric delamination. In addition, the uplift of the Gongga Mountains, the intrusion of Late Miocene granites and the activity of XSHF during this time are all suggested to be related to the lithospheric delamination (H. Li & Zhang, 2013; Y. Z. Zhang, Replumaz, et al., 2017; W. Wang et al., 2021). Indeed, one recent geochemical study (M. Zhang et al., 2021) identifies high mantle-source volatiles along the fault zone, arguing the important role XSHF played on the lithospheric scale deformation. Our model reveals significant low velocities along the XSHF at 65 km depth (Figure 9f), which might represent localized upwelling mantle materials that are still actively migrating along the fault zone. This further supports the possible delamination process in the northern part of the region beneath the NCDB and SGB.

Different from the sporadic low velocity in the north, the region south of 26°N shows a broad low velocity area in the upper mantle (65–150 km) with some particularly concentrated velocity reductions. For example, at 65 km depth (Figure 9f), the most significant velocity reduction concentrates beneath the Tengchong volcanic zone. These regions host a large amount of Cenozoic magmatism, highlighting their connection with upper mantle dynamic processes (J. Deng et al., 2014; Guo et al., 2005; C. Z. Liu et al., 2013; J. H. Wang, Yin, et al., 2001). In particular, geochronological data indicates two main phases of Cenozoic magmatism in the eastern Indo-Asian collisional zone, one from the Middle Eocene to the Early Oligocene (42–24 Ma) and the other after the Late Miocene (<16 Ma) (J. H. Wang, Yin, et al., 2001). The early potassic magmatism is mainly distributed in a 200 km wide zone across the RRF south of 26°N, which is suggested to be triggered by the delamination of the thickened lithosphere according to some geochemical evidence (B. Chen et al., 2017; Lu et al., 2015). The thinner lithosphere in the broad region south of 26°N in our model generally supports this scenario. In addition, one recent seismic study reveals high-velocity anomalies in the MTZ (Figure 11), which is interpreted as the delaminated lithosphere (Feng et al., 2022). The widespread low velocities in the upper mantle south of 26°N correspond well with the locations of the observed sinking lithosphere (profile EE' and FF' in Figure 11), indicating the close relationship between the lithospheric thickening and related delamination from continental collision and the early Cenozoic magmatism. We note that parts of the high-velocity anomalies in the MTZ occur at the north of 26°N (profile EE'), where the upper mantle low velocity is absent. Feng

et al. (2022) suggest that the shallow lithosphere within the study region might have moved southward after the lithospheric delamination, and this plate motion is still ongoing as indicated by the GPS observations. Therefore, the shallow thinned lithosphere and the deep delaminated lithosphere could have been situated in different locations.

The late potassic magmatism is mainly distributed around the Tengchong volcano, the LP-SMB and the southern part of the RRF (J. Deng et al., 2014; Guo et al., 2015), which is broadly coincident with the LVZ in the uppermost mantle (e.g., 65 km) in our model (Figure 9f). This LVZ may be caused by the upwelling of wet and hot asthenosphere material associated with the dehydration of the stagnant Indian slab in the MTZ (Z. Huang et al., 2019; Lei & Zhao, 2016) or the mantle flow related to the slab rollback (Rao & Kalpna, 2005; Sternai et al., 2014). However, our model loses resolution at depths deeper than 250 km, making it difficult to decipher its origin. Nevertheless, both mechanisms are closely related to the eastward subduction of the Indian plate. The joint inversion of teleseismic body wave traveltime data with the surface wave data might provide more information on the origin of this mantle upwelling and will be the subject of our future work.

5. Conclusion

In this study, we construct a high-resolution 3D S-wave velocity model of the crust and upper mantle beneath the broad SET region through jointly inverting Rayleigh wave phase velocities and teleseismic body-wave data. The dense and large-scale station coverage and the complementary sensitivity of surface wave and body wave to the velocity and interface structures allow us to reveal finer seismic structures in this region than previous studies.

We identify three isolated low-velocity regions in the mid-lower crust that might represent mechanically weak zones, different from connected features of these LVZs observed previously. The LVZ from the Tibetan Plateau is confined to the west of the LXF and crosses the ZDF to the south. However, it terminates well before reaching the Tengchong volcano, where an independent LVZ exists in the mid-lower crust. The LVZ around the XJF is clearly separated from the one beneath the Tibetan Plateau by high-velocity blocks beneath the YC and the ELIP. This low-velocity region is restricted to the north of the RRF, and is likely associated with the crustal thickening under the southeastward plateau expansion, mantle upwelling, and shear heating of strike-slip faults.

In the upper mantle, the local low-velocity anomalies in the NCDB and the SGB may reveal mantle upwelling related to lithospheric delamination, probably due to the compressional thickening of lithospheric material extrusion from the Tibetan Plateau. In the south of our study area, where two major phases of Cenozoic magmatism occurred in the past, we suggest two phases of tectonic events to form the low-velocity upper mantle. The first phase is the early Cenozoic lithospheric delamination caused by continental collision and thickening, which occurs over a wide area south of 26°N. The second phase may be related to the subduction of the Indian plate under the Burma arc, resulting in some localized upper mantle upwelling, forming concentrated low velocities beneath the Tengchong volcano.

Appendix A: Interpolation-Based Inversion Method

We perform the interpolation-based inversion method of Niu et al. (2007) to get smoother interfaces from all measurements. We solved the damped least squares problem to minimize the misfit function,

$$||Gm - d||^2 + \lambda^2 ||Lm||^2,$$

where m is the unknown parameters at all grid nodes, d is the measurements at all stations, G is the kernel matrix with the none zero elements corresponding to the measurements, L is the finite difference operator for the first derivative of the model, and λ is the regularization parameter. We select λ that minimize the misfit function and satisfy the following condition:

$$\sum \frac{(Gm - d)^2}{\sigma^2} = 1.$$

σ is the uncertainty of measurements, which is the standard deviation of the posterior distribution in the inversion.

Data Availability Statement

Seismic data of western Sichuan and ChinArray-Himalaya Phase I are from China Seismic Array Data Management Center at Institute of Geophysics, CEA (China Earthquake Administration) (ChinArray DMC, http://doi.org/10.17616/R31NJMMK), which can be accessed from http://www.chinarraydmc.cn/. The ambient noise cross-correlations, teleseismic surface wave waveforms, teleseismic body wave waveforms, and phase

velocity dispersion data used in this study are available from the data repository (https://doi.org/10.6084/m9.figshare.21646931.v1). The final 3D V_s model are archived and available from the data repository (https://doi.org/10.6084/m9.figshare.21586215.v1).

Acknowledgments
This work is supported by the National Science Foundation of China (NSFC, Nos. 42074055 and 41874058) and supported by MOST Special Fund from the State Key Laboratory of Geological Processes and Mineral Resources and by the Fundamental Research Funds for the Central Universities, China University of Geosciences (MSFGPMR2022-4). X. Yang is supported by China Scholarship Council.

References

Bai, D., Unsworth, M. J., Meju, M. A., Ma, X., Teng, J., Kong, X., et al. (2010). Crustal deformation of the eastern Tibetan plateau revealed by magnetotelluric imaging. *Nature Geoscience*, *3*(5), 358–362. https://doi.org/10.1038/ngeo830

Bao, X., Song, X., Eaton, D. W., Xu, Y., & Chen, H. (2020). Episodic lithospheric deformation in eastern Tibet inferred from seismic anisotropy. *Geophysical Research Letters*, *47*(3), e2019GL085721. https://doi.org/10.1029/2019GL085721

Bao, X., Song, X., & Li, J. (2015). High-resolution lithospheric structure beneath Mainland China from ambient noise and earthquake surface-wave tomography. *Earth and Planetary Science Letters*, *417*, 132–141. https://doi.org/10.1016/j.epsl.2015.02.024

Bao, X., Sun, X., Xu, M., Eaton, D. W., Song, X., Wang, L., et al. (2015). Two crustal low-velocity channels beneath SE Tibet revealed by joint inversion of Rayleigh wave dispersion and receiver functions. *Earth and Planetary Science Letters*, *415*, 16–24. https://doi.org/10.1016/j.epsl.2015.01.020

Bao, Y., & Niu, F. (2017). Constraining sedimentary structure using frequency-dependent P wave particle motion: A case study of the Songliao basin in NE China. *Journal of Geophysical Research: Solid Earth*, *122*(11), 9083–9094. https://doi.org/10.1002/2017JB014721

Barmin, M. P., Ritzwoller, M. H., & Levshin, A. L. (2001). A fast and reliable method for surface wave tomography. *Pure and Applied Geophysics*, *158*(8), 1351–1375. https://doi.org/10.1007/PL00001225

Bassin, C., Laske, G., & Masters, G. (2000). The current limits of resolution for surface wave tomography in North America. *EOS Transactions AGU*, *81*, F897.

Beaumont, C., Jamieson, R. A., Nguyen, M. H., & Medvedev, S. (2004). Crustal channel flows: 1. Numerical models with applications to the tectonics of the Himalayan-Tibetan orogen. *Journal of Geophysical Research*, *109*(B6), B06406. https://doi.org/10.1029/2003JB002809

Bensen, G. D., Ritzwoller, M. H., Barmin, M. P., Levshin, A. L., Lin, F., Moschetti, M. P., et al. (2007). Processing seismic ambient noise data to obtain reliable broad-band surface wave dispersion measurements. *Geophysical Journal International*, *169*(3), 1239–1260. https://doi.org/10.1111/j.1365-246X.2007.03374.x

Birch, F. (1961). The velocity of compressional waves in rocks to 10 kilobars: 2. *Journal of Geophysical Research*, *66*(7), 2199–2224. https://doi.org/10.1029/JZ066i007p02199

Bodin, T., Sambridge, M., Rawlinson, N., & Arroucau, P. (2012). Transdimensional tomography with unknown data noise. *Geophysical Journal International*, *189*(3), 1536–1556. https://doi.org/10.1111/j.1365-246X.2012.05414.x

Bodin, T., Yuan, H., & Romanowicz, B. (2014). Inversion of receiver functions without deconvolution—Application to the Indian craton. *Geophysical Journal International*, *196*(2), 1025–1033. https://doi.org/10.1093/gji/ggt431

Brocher, T. M. (2005). Empirical relations between elastic wavespeeds and density in the Earth's crust. *Bulletin of the Seismological Society of America*, *95*(6), 2081–2092. https://doi.org/10.1785/0120050077

Chen, B., Long, X., Wilde, S. A., Yuan, C., Wang, Q., Xia, X., & Zhang, Z. (2017). Delamination of lithospheric mantle evidenced by cenozoic potassic rocks in Yunnan, SW China: A contribution to uplift of the eastern Tibetan Plateau. *Lithos*, *284*, 709–729. https://doi.org/10.1016/j.lithos.2017.05.019

Chen, F., Satir, M., Ji, J., & Zhong, D. (2002). Nd–Sr–Pb isotopes of Tengchong cenozoic volcanic rocks from western Yunnan, China: Evidence for an enriched-mantle source. *Journal of Asian Earth Sciences*, *21*(1), 39–45. https://doi.org/10.1016/S1367-9120(02)00007-X

Chen, H., Zhu, L., & Su, Y. (2016). Low velocity crustal flow and crust–mantle coupling mechanism in Yunnan, SE Tibet, revealed by 3D S-wave velocity and azimuthal anisotropy. *Tectonophysics*, *685*, 8–20. https://doi.org/10.1016/j.tecto.2016.07.007

Chen, L., Song, X., Gerya, T. V., Xu, T., & Chen, Y. (2019). Crustal melting beneath orogenic plateaus: Insights from 3-D thermo-mechanical modeling. *Tectonophysics*, *761*, 1–15. https://doi.org/10.1016/j.tecto.2019.03.014

Chen, M., Huang, H., Yao, H., van der Hilst, R., & Niu, F. (2014). Low wave speed zones in the crust beneath SE Tibet revealed by ambient noise adjoint tomography. *Geophysical Research Letters*, *41*(2), 334–340. https://doi.org/10.1002/2013GL058476

Chen, Y., Xu, Y., Xu, T., Si, S., Liang, X., Tian, X., et al. (2015). Magmatic underplating and crustal growth in the Emeishan Large Igneous Province, SW China, revealed by a passive seismic experiment. *Earth and Planetary Science Letters*, *432*, 103–114. https://doi.org/10.1016/j.epsl.2015.09.048

ChinArray. (2006). *Waveform data of China seismic array*. China Earthquake Administration. https://doi.org/10.12001/ChinArray.Data

Clark, M. K., & Royden, L. H. (2000). Topographic ooze: Building the eastern margin of Tibet by lower crustal flow. *Geology*, *28*(8), 703–706. https://doi.org/10.1130/0091-7613(2000)28<703:TOBTEM>2.0.CO;2

Cook, K. L., & Royden, L. H. (2008). The role of crustal strength variations in shaping orogenic plateaus, with application to Tibet. *Journal of Geophysical Research*, *113*(B8), B08407. https://doi.org/10.1029/2007JB005457

Deng, J., Wang, Q., Li, G., & Santosh, M. (2014). Cenozoic tectono-magmatic and metallogenic processes in the Sanjiang region, southwestern China. *Earth-Science Reviews*, *138*, 268–299. https://doi.org/10.1016/j.earscirev.2014.05.015

Deng, Y., Chen, Y., Wang, P., Essa, K. S., Xu, T., Liang, X., & Badal, J. (2016). Magmatic underplating beneath the Emeishan large igneous province (South China) revealed by the COMGRA-ELIP experiment. *Tectonophysics*, *672–673*, 16–23. https://doi.org/10.1016/j.tecto.2016.01.039

Duan, X. Z., Fan, H. R., Zhang, H. F., Yaxley, G., Santosh, M., Tian, H. C., et al. (2019). Melt inclusions in phenocrysts track enriched upper mantle source for Cenozoic Tengchong volcanic field, Yunnan Province, SW China. *Lithos*, *324*, 180–201. https://doi.org/10.1016/j.lithos.2018.10.034

Dziewonski, A. M., & Anderson, D. L. (1981). Preliminary reference Earth model. *Physics of the Earth and Planetary Interiors*, *25*(4), 297–356. https://doi.org/10.1016/0031-9201(81)90046-7

Feng, J., Yao, H., Chen, L., & Wang, W. (2022). Massive lithospheric delamination in southeastern Tibet facilitating continental extrusion. *National Science Review*, *9*(4), nwab174. https://doi.org/10.1093/nsr/nwab174

Forsyth, D. W., & Li, A. (2005). Array analysis of two-dimensional variations in surface wave phase velocity and azimuthal anisotropy in the presence of multipathing interference. *Seismic Earth: Array Analysis of Broadband Seismograms*, *157*, 81–97. https://doi.org/10.1029/157GM06

Fu, Y. V., Gao, Y., Li, A., Li, L., & Chen, A. (2017). Lithospheric structure of the southeastern margin of the Tibetan Plateau from Rayleigh wave tomography. *Journal of Geophysical Research: Solid Earth*, *122*(6), 4631–4644. https://doi.org/10.1002/2016JB013096

Gardner, G. H. F., Gardner, L. W., & Gregory, A. (1974). Formation velocity and density—The diagnostic basics for stratigraphic traps. *Geophysics*, *39*(6), 770–780. https://doi.org/10.1190/1.1440465

Guo, Z., Cheng, Z., Zhang, M., Zhang, L., Li, X., & Liu, J. (2015). Post-collisional high-K calc-alkaline volcanism in Tengchong volcanic field, SE Tibet: Constraints on Indian eastward subduction and slab detachment. *Journal of the Geological Society*, *172*(5), 624–640. https://doi.org/10.1144/jgs2014-078

Guo, Z., Hertogen, J., Liu, J., Pasteels, P., Boven, A., Punzalan, L., et al. (2005). Potassic magmatism in western Sichuan and Yunnan provinces, SE Tibet, China: Petrological and geochemical constraints on petrogenesis. *Journal of Petrology*, *46*(1), 33–78. https://doi.org/10.1093/petrology/egh061

Haario, H., Laine, M., Mira, A., & Saksman, E. (2006). DRAM: Efficient adaptive MCMC. *Statistics and Computing*, *16*(4), 339–354. https://doi.org/10.1007/s11222-006-9438-0

Hafkenscheid, E., Wortel, M. J. R., & Spakman, W. (2006). Subduction history of the Tethyan region derived from seismic tomography and tectonic reconstructions. *Journal of Geophysical Research*, *111*(B8), B08401. https://doi.org/10.1029/2005JB003791

Han, C., Huang, Z., Hao, S., Wang, L., Xu, M., & Hammond, J. O. (2022). Restricted lithospheric extrusion in the SE Tibetan Plateau: Evidence from anisotropic Rayleigh-wave tomography. *Earth and Planetary Science Letters*, *598*, 117837. https://doi.org/10.1016/j.epsl.2022.117837

Han, C., Xu, M., Huang, Z., Wang, L., Xu, M., Mi, N., et al. (2020). Layered crustal anisotropy and deformation in the SE Tibetan plateau revealed by Markov-Chain-Monte-Carlo inversion of receiver functions. *Physics of the Earth and Planetary Interiors*, *306*, 106522. https://doi.org/10.1016/j.pepi.2020.106522

Hao, M., Freymueller, J. T., Wang, Q., Cui, D., & Qin, S. (2016). Vertical crustal movement around the southeastern Tibetan Plateau constrained by GPS and GRACE data. *Earth and Planetary Science Letters*, *437*, 1–8. https://doi.org/10.1016/j.epsl.2015.12.038

Harrison, T. M., Copeland, P., Kidd, W. S. F., & Yin, A. N. (1992). Raising Tibet. *Science*, *255*(5052), 1663–1670. https://doi.org/10.1126/science.255.5052.1663

Haskell, N. A. (1962). Crustal reflection of plane P and SV waves. *Journal of Geophysical Research*, *67*(12), 4751–4768. https://doi.org/10.1029/JZ067i012p04751

Herrmann, R. B. (2013). Computer programs in seismology: An evolving tool for instruction and research. *Seismological Research Letters*, *84*(6), 1081–1088. https://doi.org/10.1785/0220110096

Hoke, G. D., Liu-Zeng, J., Hren, M. T., Wissink, G. K., & Garzione, C. N. (2014). Stable isotopes reveal high southeast Tibetan Plateau margin since the Paleogene. *Earth and Planetary Science Letters*, *394*, 270–278. https://doi.org/10.1016/j.epsl.2014.03.007

Houseman, G. A., McKenzie, D. P., & Molnar, P. (1981). Convective instability of a thickened boundary layer and its relevance for the thermal evolution of continental convergent belts. *Journal of Geophysical Research*, *86*(B7), 6115–6132. https://doi.org/10.1029/JB086iB07p06115

Hu, S., He, L., & Wang, J. (2000). Heat flow in the continental area of China: A new data set. *Earth and Planetary Science Letters*, *179*(2), 407–419. https://doi.org/10.1016/S0012-821X(00)00126-6

Huang, H., Yao, H., & van der Hilst, R. D. (2010). Radial anisotropy in the crust of SE Tibet and SW China from ambient noise interferometry. *Geophysical Research Letters*, *37*(21), L21310. https://doi.org/10.1029/2010GL044981

Huang, Z., Wang, L., Xu, M., & Zhao, D. (2018). P wave anisotropic tomography of the SE Tibetan Plateau: Evidence for the crustal and upper-mantle deformations. *Journal of Geophysical Research: Solid Earth*, *123*(10), 8957–8978. https://doi.org/10.1029/2018JB016048

Huang, Z., Wang, L., Xu, M., Zhao, D., Mi, N., & Yu, D. (2019). P and S wave tomography beneath the SE Tibetan Plateau: Evidence for lithospheric delamination. *Journal of Geophysical Research: Solid Earth*, *124*(10), 10292–10308. https://doi.org/10.1029/2019JB017430

Huang, Z., Wang, P., Xu, M., Wang, L., Ding, Z., Wu, Y., et al. (2015). Mantle structure and dynamics beneath SE Tibet revealed by new seismic images. *Earth and Planetary Science Letters*, *411*, 100–111. https://doi.org/10.1016/j.epsl.2014.11.040

Jiang, G., Hu, S., Shi, Y., Zhang, C., Wang, Z., & Hu, D. (2019). Terrestrial heat flow of continental China: Updated dataset and tectonic implications. *Tectonophysics*, *753*, 36–48. https://doi.org/10.1016/j.tecto.2019.01.006

Kennett, B. L., Engdahl, E. R., & Buland, R. (1995). Constraints on seismic velocities in the Earth from traveltimes. *Geophysical Journal International*, *122*(1), 108–124. https://doi.org/10.1111/j.1365-246X.1995.tb03540.x

Lee, H. Y., Chung, S. L., & Yang, H. M. (2016). Late Cenozoic volcanism in central Myanmar: Geochemical characteristics and geodynamic significance. *Lithos*, *245*, 174–190. https://doi.org/10.1016/j.lithos.2015.09.018

Lee, T.-Y., & Lawver, L. A. (1995). Cenozoic plate reconstruction of Southeast Asia. *Tectonophysics*, *251*(1–4), 85–138. https://doi.org/10.1016/0040-1951(95)00023-2

Lei, J., & Zhao, D. (2016). Teleseismic P-wave tomography and mantle dynamics beneath Eastern Tibet. *Geochemistry, Geophysics, Geosystems*, *17*(5), 1861–1884. https://doi.org/10.1002/2016GC006262

Lei, J., Zhao, D., Xu, X., Xu, Y. G., & Du, M. (2019). Is there a big mantle wedge under eastern Tibet? *Physics of the Earth and Planetary Interiors*, *292*, 100–113. https://doi.org/10.1016/j.pepi.2019.04.005

Leloup, P. H., Ricard, Y., Battaglia, J., & Lacassin, R. (1999). Shear heating in continental strike-slip shear zones: Model and field examples. *Geophysical Journal International*, *136*(1), 19–40. https://doi.org/10.1046/j.1365-246X.1999.00683.x

Levshin, A. L., & Ritzwoller, M. H. (2001). Automated detection, extraction, and measurement of regional surface waves. *Pure and Applied Geophysics*, *158*(8), 1531–1545. https://doi.org/10.1007/PL00001233

Li, G., Niu, F., Yang, Y., & Tao, K. (2019). Joint inversion of Rayleigh wave phase velocity, particle motion, and teleseismic body wave data for sedimentary structures. *Geophysical Research Letters*, *46*(12), 6469–6478. https://doi.org/10.1029/2019GL082746

Li, G., Niu, F., Yang, Y., & Xie, J. (2018). An investigation of time–frequency domain phase-weighted stacking and its application to phase-velocity extraction from ambient noise's empirical Green's functions. *Geophysical Journal International*, *212*(2), 1143–1156. https://doi.org/10.1093/gji/ggx448

Li, G., Yang, Y., Niu, F., & Chen, M. (2021). 3-D sedimentary structures beneath southeastern Australia constrained by passive seismic array data. *Journal of Geophysical Research: Solid Earth*, *126*(2), e2020JB019998. https://doi.org/10.1029/2020JB019998

Li, H., Su, W., Wang, C. Y., & Huang, Z. (2009). Ambient noise Rayleigh wave tomography in western Sichuan and eastern Tibet. *Earth and Planetary Science Letters*, *282*(1–4), 201–211. https://doi.org/10.1016/j.epsl.2009.03.021

Li, H., & Zhang, Y. (2013). Zircon U–Pb geochronology of the Konggar granitoid and migmatite: Constraints on the Oligo-Miocene tectono-thermal evolution of the Xianshuihe fault zone, East Tibet. *Tectonophysics*, *606*, 127–139. https://doi.org/10.1016/j.tecto.2013.07.007

Li, M., Zhang, S., Wang, F., Wu, T., & Qin, W. (2016). Crustal and upper-mantle structure of the southeastern Tibetan Plateau from joint analysis of surface wave dispersion and receiver functions. *Journal of Asian Earth Sciences*, *117*, 52–63. https://doi.org/10.1016/j.jseaes.2015.12.002

Li, S., Currie, B. S., Rowley, D. B., & Ingalls, M. (2015). Cenozoic paleoaltimetry of the SE margin of the Tibetan Plateau: Constraints on the tectonic evolution of the region. *Earth and Planetary Science Letters*, *432*, 415–424. https://doi.org/10.1016/j.epsl.2015.09.044

Li, X., Bai, D., Ma, X., Chen, Y., Varentsov, I. M., Xue, G., et al. (2019). Electrical resistivity structure of the Xiaojiang strike-slip fault system (SW China) and its tectonic implications. *Journal of Asian Earth Sciences*, *176*, 57–67. https://doi.org/10.1016/j.jseaes.2019.01.031

Li, X., Ma, X., Chen, Y., Xue, S., Varentsov, I. M., & Bai, D. (2020). A plume-modified lithospheric barrier to the southeastward flow of partially molten Tibetan crust inferred from magnetotelluric data. *Earth and Planetary Science Letters*, *548*, 116493. https://doi.org/10.1016/j.epsl.2020.116493

Liu, C. Z., Wu, F. Y., Sun, J., Chu, Z. Y., & Yu, X. H. (2013). Petrology, geochemistry and ReOs isotopes of peridotite xenoliths from Maguan, Yunnan Province: Implications for the Cenozoic mantle replacement in southwestern China. *Lithos*, *168*, 1–14. https://doi.org/10.1016/j.lithos.2013.01.011

Liu, M., Cui, X., & Liu, F. (2004). Cenozoic rifting and volcanism in eastern China: A mantle dynamic link to the Indo–Asian collision? *Tectonophysics*, *393*(1–4), 29–42. https://doi.org/10.1016/j.tecto.2004.07.029

Liu, Q. Y., Van Der Hilst, R. D., Li, Y., Yao, H. J., Chen, J. H., Guo, B., et al. (2014). Eastward expansion of the Tibetan Plateau by crustal flow and strain partitioning across faults. *Nature Geoscience*, *7*(5), 361–365. https://doi.org/10.1038/ngeo2130

Liu, Y., Li, L., van Wijk, J., Li, A., & Fu, Y. V. (2021). Surface-wave tomography of the Emeishan large igneous province (China): Magma storage system, hidden hotspot track, and its impact on the Capitanian mass extinction. *Geology*, *49*(9), 1032–1037. https://doi.org/10.1130/G49055.1

Liu, Y., Yao, H., Zhang, H., & Fang, H. (2021). The community velocity model V. 1.0 of southwest China, constructed from joint body-and surface-wave travel-time tomography. *Seismological Research Letters*, *92*(5), 2972–2987. https://doi.org/10.1785/0220200318

Lu, Y. J., McCuaig, T. C., Li, Z. X., Jourdan, F., Hart, C. J., Hou, Z. Q., & Tang, S. H. (2015). Paleogene post-collisional lamprophyres in western Yunnan, western Yangtze craton: Mantle source and tectonic implications. *Lithos*, *233*, 139–161. https://doi.org/10.1016/j.lithos.2015.02.003

Luo, Y., Yang, Y., Xu, Y., Xu, H., Zhao, K., & Wang, K. (2015). On the limitations of interstation distances in ambient noise tomography. *Geophysical Journal International*, *201*(2), 652–661. https://doi.org/10.1093/gji/ggv043

McKenzie, D., & Priestley, K. (2008). The influence of lithospheric thickness variations on continental evolution. *Lithos*, *102*(1–2), 1–11. https://doi.org/10.1016/j.lithos.2007.05.005

Menke, W., & Levin, V. (2003). The cross-convolution method for interpreting SKS splitting observations, with application to one and two-layer anisotropic Earth models. *Geophysical Journal International*, *154*(2), 379–392. https://doi.org/10.1046/j.1365-246X.2003.01937.x

Molnar, P., & Tapponnier, P. (1975). Cenozoic Tectonics of Asia: Effects of a Continental Collision: Features of recent continental tectonics in Asia can be interpreted as results of the India-Eurasia collision. *Science*, *189*(4201), 419–426. https://doi.org/10.1126/science.189.4201.419

Ni, J. F., Guzman-Speziale, M., Bevis, M., Holt, W. E., Wallace, T. C., & Seager, W. R. (1989). Accretionary tectonics of Burma and the three-dimensional geometry of the Burma subduction zone. *Geology*, *17*(1), 68–71. https://doi.org/10.1130/0091-7613(1989)017<0068:ATOBAT>2.3.CO;2

Niu, F., Bravo, T., Pavlis, G., Vernon, F., Rendon, H., Bezada, M., & Levander, A. (2007). Receiver function study of the crustal structure of the southeastern Caribbean plate boundary and Venezuela. *Journal of Geophysical Research*, *112*(B11), B11308. https://doi.org/10.1029/2006JB004802

Pan, Y., & Shen, W. B. (2017). Contemporary crustal movement of southeastern Tibet: Constraints from dense GPS measurements. *Scientific Reports*, *7*(1), 1–7. https://doi.org/10.1038/srep45348

Qiao, L., Yao, H., Lai, Y. C., Huang, B. S., & Zhang, P. (2018). Crustal structure of Southwest China and northern Vietnam from ambient noise tomography: Implication for the large-scale material transport model in SE Tibet. *Tectonics*, *37*(5), 1492–1506. https://doi.org/10.1029/2018TC004957

Rao, N. P., & Kalpna (2005). Deformation of the subducted Indian lithospheric slab in the Burmese arc. *Geophysical Research Letters*, *32*(5), L05301. https://doi.org/10.1029/2004GL022034

Replumaz, A., Karason, H., van der Hilst, R. D., Besse, J., & Tapponnier, P. (2004). 4-D evolution of SE Asia's mantle from geological reconstructions and seismic tomography. *Earth and Planetary Science Letters*, *221*(1–4), 103–115. https://doi.org/10.1016/S0012-821X(04)00070-6

Richards, S., Lister, G., & Kennett, B. (2007). A slab in depth: Three-dimensional geometry and evolution of the Indo-Australian plate. *Geochemistry, Geophysics, Geosystems*, *8*(12), Q12003. https://doi.org/10.1029/2007GC001657

Rowley, D. B. (1996). Age of initiation of collision between India and Asia: A review of stratigraphic data. *Earth and Planetary Science Letters*, *145*(1–4), 1–13. https://doi.org/10.1016/S0012-821X(96)00201-4

Royden, L. H., Burchfiel, B. C., King, R. W., Wang, E., Chen, Z., Shen, F., & Liu, Y. (1997). Surface deformation and lower crustal flow in eastern Tibet. *Science*, *276*(5313), 788–790. https://doi.org/10.1126/science.276.5313.788

Royden, L. H., Burchfiel, B. C., & van der Hilst, R. D. (2008). The geological evolution of the Tibetan Plateau. *Science*, *321*(5892), 1054–1058. https://doi.org/10.1126/science.1155371

Schimmel, M., & Gallart, J. (2007). Frequency-dependent phase coherence for noise suppression in seismic array data. *Journal of Geophysical Research*, *112*(B4), B04303. https://doi.org/10.1029/2006JB004680

Schott, B., & Schmeling, H. (1998). Delamination and detachment of a lithospheric root. *Tectonophysics*, *296*(3–4), 225–247. https://doi.org/10.1016/S0040-1951(98)00154-1

Shen, W., Ritzwoller, M. H., Kang, D., Kim, Y., Lin, F. C., Ning, J., et al. (2016). A seismic reference model for the crust and uppermost mantle beneath China from surface wave dispersion. *Geophysical Journal International*, *206*(2), 954–979. https://doi.org/10.1093/gji/ggw175

Shen, Z.-K., Lü, J., Wang, M., & Bürgmann, R. (2005). Contemporary crustal deformation around the southeast borderland of the Tibetan Plateau. *Journal of Geophysical Research*, *110*(B11), B11409. https://doi.org/10.1029/2004JB003421

Sternai, P., Jolivet, L., Menant, A., & Gerya, T. (2014). Driving the upper plate surface deformation by slab rollback and mantle flow. *Earth and Planetary Science Letters*, *405*, 110–118. https://doi.org/10.1016/j.epsl.2014.08.023

Sun, Y., Niu, F., Liu, H., Chen, Y., & Liu, J. (2012). Crustal structure and deformation of the SE Tibetan plateau revealed by receiver function data. *Earth and Planetary Science Letters*, *349*, 186–197. https://doi.org/10.1016/j.epsl.2012.07.007

Tao, K., Grand, S. P., & Niu, F. (2018). Seismic structure of the upper mantle beneath eastern Asia from full waveform seismic tomography. *Geochemistry, Geophysics, Geosystems*, *19*(8), 2732–2763. https://doi.org/10.1029/2018GC007460

Tapponnier, P., Peltzer, G., Le Dain, A. Y., Armijo, R., & Cobbold, P. (1982). Propagating extrusion tectonics in Asia: New insights from simple experiments with plasticine. *Geology*, *10*(12), 611–616. https://doi.org/10.1130/0091-7613(1982)10<611:PETIAN>2.0.CO;2

Tapponnier, P., Xu, Z., Roger, F., Meyer, B., Arnaud, N., Wittlinger, G., & Yang, J. (2001). Oblique stepwise rise and growth of the Tibet Plateau. *Science*, *294*(5547), 1671–1677. https://doi.org/10.1126/science.105978

Thomson, W. T. (1950). Transmission of elastic waves through a stratified solid medium. *Journal of Applied Physics*, *21*(2), 89–93. https://doi.org/10.1063/1.1699629

Tian, H. C., Yang, W., Li, S. G., Ke, S., & Duan, X. Z. (2018). Low δ^{26}Mg volcanic rocks of Tengchong in southwestern China: A deep carbon cycle induced by supercritical liquids. *Geochimica et Cosmochimica Acta*, *240*, 191–219. https://doi.org/10.1016/j.gca.2018.08.032

Wang, C. Y., Chan, W. W., & Mooney, W. D. (2003). Three-dimensional velocity structure of crust and upper mantle in southwestern China and its tectonic implications. *Journal of Geophysical Research*, *108*(B9), 2442. https://doi.org/10.1029/2002JB001973

Wang, C. Y., Flesch, L. M., Chang, L., & Zheng, T. (2013). Evidence of active mantle flow beneath South China. *Geophysical Research Letters*, *40*(19), 5137–5141. https://doi.org/10.1002/grl.50987

Wang, C. Y., Wu, J., Lou, H., Zhou, M., & Bai, Z. (2003). P-wave crustal velocity structure in western Sichuan and eastern Tibetan region. *Science in China Series D: Earth Sciences*, *46*(2), 254–265. https://doi.org/10.1360/03dz0020

Wang, G., Wan, J., Wang, E., Zheng, D., & Li, F. (2008). Late Cenozoic to recent transtensional deformation across the Southern part of the Gaoligong shear zone between the Indian plate and SE margin of the Tibetan plateau and its tectonic origin. *Tectonophysics*, *460*(1–4), 1–20. https://doi.org/10.1016/j.tecto.2008.04.007

Wang, J. H., Yin, A., Harrison, T. M., Grove, M., Zhang, Y. Q., & Xie, G. H. (2001). A tectonic model for Cenozoic igneous activities in the eastern Indo–Asian collision zone. *Earth and Planetary Science Letters*, *188*(1–2), 123–133. https://doi.org/10.1016/S0012-821X(01)00315-6

Wang, M., Hubbard, J., Plesch, A., Shaw, J. H., & Wang, L. (2016). Three-dimensional seismic velocity structure in the Sichuan basin, China. *Journal of Geophysical Research: Solid Earth*, *121*(2), 1007–1022. https://doi.org/10.1002/2015JB012644

Wang, M., & Shen, Z. K. (2020). Present-day crustal deformation of continental China derived from GPS and its tectonic implications. *Journal of Geophysical Research: Solid Earth*, *125*(2), e2019JB018774. https://doi.org/10.1029/2019JB018774

Wang, Q., Zhang, P. Z., Freymueller, J. T., Bilham, R., Larson, K. M., Lai, X. A., et al. (2001). Present-day crustal deformation in China constrained by global positioning system measurements. *Science*, *294*(5542), 574–577. https://doi.org/10.1126/science.1063647

Wang, W., Wu, J., Fang, L., Lai, G., & Cai, Y. (2017). Crustal thickness and Poisson's ratio in southwest China based on data from dense seismic arrays. *Journal of Geophysical Research: Solid Earth*, *122*(9), 7219–7235. https://doi.org/10.1002/2017JB013978

Wang, W., Wu, J., & Hammond, J. O. (2021). Mantle dynamics beneath the Sichuan Basin and eastern Tibet from teleseismic tomography. *Tectonics*, *40*(2), e2020TC006319. https://doi.org/10.1029/2020TC006319

Xie, J., Ritzwoller, M. H., Shen, W., & Wang, W. (2017). Crustal anisotropy across eastern Tibet and surroundings modeled as a depth-dependent tilted hexagonally symmetric medium. *Geophysical Journal International*, *209*(1), 466–491. https://doi.org/10.1093/gji/ggx004

Xie, J., Ritzwoller, M. H., Shen, W., Yang, Y., Zheng, Y., & Zhou, L. (2013). Crustal radial anisotropy across eastern Tibet and the western Yangtze craton. *Journal of Geophysical Research: Solid Earth*, *118*(8), 4226–4252. https://doi.org/10.1002/jgrb.50296

Xu, M., Huang, H., Huang, Z., Wang, P., Wang, L., Xu, M., et al. (2018). Insight into the subducted Indian slab and origin of the Tengchong volcano in SE Tibet from receiver function analysis. *Earth and Planetary Science Letters*, *482*, 567–579. https://doi.org/10.1016/j.epsl.2017.11.048

Yang, Y., & Forsyth, D. W. (2006a). Rayleigh wave phase velocities, small-scale convection, and azimuthal anisotropy beneath southern California. *Journal of Geophysical Research*, *111*(B7), B07306. https://doi.org/10.1029/2005JB004180

Yang, Y., & Forsyth, D. W. (2006b). Regional tomographic inversion of the amplitude and phase of Rayleigh waves with 2-D sensitivity kernels. *Geophysical Journal International*, *166*(3), 1148–1160. https://doi.org/10.1111/j.1365-246X.2006.02972.x

Yang, Y., Ritzwoller, M. H., Zheng, Y., Shen, W., Levshin, A. L., & Xie, Z. (2012). A synoptic view of the distribution and connectivity of the mid-crustal low velocity zone beneath Tibet. *Journal of Geophysical Research*, *117*(B4), B04303. https://doi.org/10.1029/2011JB008810

Yang, Y., Yao, H., Wu, H., Zhang, P., & Wang, M. (2020). A new crustal shear-velocity model in Southwest China from joint seismological inversion and its implications for regional crustal dynamics. *Geophysical Journal International*, *220*(2), 1379–1393. https://doi.org/10.1093/gji/ggz514

Yao, H., Beghein, C., & Van Der Hilst, R. D. (2008). Surface wave array tomography in SE Tibet from ambient seismic noise and two-station analysis-II. Crustal and upper-mantle structure. *Geophysical Journal International*, *173*(1), 205–219. https://doi.org/10.1111/j.1365-246X.2007.03696.x

Yao, H., Van Der Hilst, R. D., & Montagner, J. P. (2010). Heterogeneity and anisotropy of the lithosphere of SE Tibet from surface wave array tomography. *Journal of Geophysical Research*, *115*(B12), B12307. https://doi.org/10.1029/2009JB007142

Yin, A., & Harrison, T. M. (2000). Geologic evolution of the Himalayan-Tibetan orogen. *Annual Review of Earth and Planetary Sciences*, *28*(1), 211–280. https://doi.org/10.1146/annurev.earth.28.1.211

Zeng, S., Zheng, Y., Niu, F., & Ai, S. (2021). Measurements of seismometer orientation of the first phase CHINArray and their implications on vector-recording-based seismic studies. *Bulletin of the Seismological Society of America*, *111*(1), 36–49. https://doi.org/10.1785/0120200129

Zhang, M., Guo, Z., Xu, S., Barry, P. H., Sano, Y., Zhang, L., et al. (2021). Linking deeply-sourced volatile emissions to plateau growth dynamics in southeastern Tibetan Plateau. *Nature Communications*, *12*(1), 4517. https://doi.org/10.1038/s41467-021-24415-y

Zhang, P. Z. (2013). A review on active tectonics and deep crustal processes of the Western Sichuan region, eastern margin of the Tibetan Plateau. *Tectonophysics*, *584*, 7–22. https://doi.org/10.1016/j.tecto.2012.02.021

Zhang, P. Z., Shen, Z., Wang, M., Gan, W., Bürgmann, R., Molnar, P., et al. (2004). Continuous deformation of the Tibetan Plateau from global positioning system data. *Geology*, *32*(9), 809–812. https://doi.org/10.1130/G20554.1

Zhang, R., Wu, Y., Gao, Z., Fu, Y. V., Sun, L., Wu, Q., & Ding, Z. (2017). Upper mantle discontinuity structure beneath eastern and southeastern Tibet: New constraints on the Tengchong intraplate volcano and signatures of detached lithosphere under the western Yangtze Craton. *Journal of Geophysical Research: Solid Earth*, *122*(2), 1367–1380. https://doi.org/10.1002/2016JB013551

Zhang, Y. Z., Replumaz, A., Leloup, P. H., Wang, G. C., Bernet, M., van der Beek, P., et al. (2017). Cooling history of the Gongga batholith: Implications for the Xianshuihe Fault and Miocene kinematics of SE Tibet. *Earth and Planetary Science Letters*, *465*, 1–15. https://doi.org/10.1016/j.epsl.2017.02.025

Zhang, Z., Yao, H., & Yang, Y. (2020). Shear wave velocity structure of the crust and upper mantle in Southeastern Tibet and its geodynamic implications. *Science China Earth Sciences*, *63*(9), 1278–1293. https://doi.org/10.1007/s11430-020-9625-3

Zhao, L.-F., Xie, X. B., He, J. K., Tian, X., & Yao, Z. X. (2013). Crustal flow pattern beneath the Tibetan Plateau constrained by regional Lg-wave Q tomography. *Earth and Planetary Science Letters*, *383*, 113–122. https://doi.org/10.1016/j.epsl.2013.09.038

Zhao, Y., Guo, L., Guo, Z., Chen, Y. J., Shi, L., & Li, Y. (2020). High resolution crustal model of SE Tibet from joint inversion of seismic P-wave travel-times and Bouguer gravity anomalies and its implication for the crustal channel flow. *Tectonophysics*, *792*, 228580. https://doi.org/10.1016/j.tecto.2020.228580

Zhao, Y., Guo, Z., Wang, K., & Yang, Y. J. (2021). A large magma reservoir beneath the Tengchong volcano revealed by ambient noise adjoint tomography. *Journal of Geophysical Research: Solid Earth*, *126*(7), e2021JB022116. https://doi.org/10.1029/2021JB022116

Zhou, M. F., Robinson, P. T., Wang, C. Y., Zhao, J. H., Yan, D. P., Gao, J. F., & Malpas, J. (2012). Heterogeneous mantle source and magma differentiation of quaternary arc-like volcanic rocks from Tengchong, SE margin of the Tibetan Plateau. *Contributions to Mineralogy and Petrology*, *163*(5), 841–860. https://doi.org/10.1007/s00410-011-0702-8